Object Recognition and Localization Using Multiple Sensors for a Robot Gripper

Master's Thesis

Stephan Johann Mühlbacher-Karrer

Supervisor:
Assoc. Prof. Dipl.-Ing. Dr. Hubert Zangl

Institute of Electrical Measurement
and Measurement Signal Processing
Graz University of Technology

Graz, February 2012

Deutsche Fassung:
Beschluss der Curricula-Kommission für Bachelor-, Master- und Diplomstudien vom 10.11.2008
Genehmigung des Senates am 1.12.2008

EIDESSTATTLICHE ERKLÄRUNG

Ich erkläre an Eides statt, dass ich die vorliegende Arbeit selbstständig verfasst, andere als die angegebenen Quellen/Hilfsmittel nicht benutzt, und die den benutzten Quellen wörtlich und inhaltlich entnommene Stellen als solche kenntlich gemacht habe.

Graz, am …………………………… ………………………………………………..
(Unterschrift)

Englische Fassung:

STATUTORY DECLARATION

I declare that I have authored this thesis independently, that I have not used other than the declared sources / resources, and that I have explicitly marked all material which has been quoted either literally or by content from the used sources.

…………………………… ………………………………………………..
date (signature)

Danksagung

Für die ausgezeichnete fachliche Betreuung zur Erstellung dieser Masterarbeit möchte ich mich bei Assoc. Prof. Dipl.-Ing. Dr. techn. Hubert Zangl und bei Dipl.-Ing. Thomas Schlegel recht herzlich bedanken.

Ein besonderer Dank gilt auch meiner gesamten Familie, die mich das gesamte Studium hindurch unterstützt hat.

Abstract

This master thesis presents a pretouch sensor system for a robot grasper. A pretouch sensor system closes the gap between long distance (e.g., vision based) and short distance (e.g., contact based) sensing. It enables the robot to recognize and localize objects before touching them. Pretouch sensor systems can be utilized for robotic applications such as grasping. The developed pretouch sensor system can be used for object recognition and localization with respect to the material properties. Two different measurement principles are investigated and combined to extend the range of objects to be sensed. The first part takes advantage of the giant magnetoresistance effect to detect ferromagnetic objects. A maximum likelihood estimator is implemented to estimate the position of the object. The second part of the thesis is inspired by the electrical capacitance tomography, which can be used to recognize and localize objects based on their relative permittivity. There a two reconstruction algorithm that are examined and shown in comparison. The prototype of the pretouch sensor system is split into two components: The first part consisting of the sensors and data acquisition hardware is mounted on the grasper. The second part contains the receiver unit and a PC utilized for the reconstruction process. The two individual components are connected wirelessly via a radio frequency link. The applicability of this approach for the pretouch sensor system is confirmed by the reconstruction results at the end of this thesis.

Keywords: Pretouch sensor system, electrical capacitance tomography, maximum likelihood estimator, grasper, object localization, giant magnetoresistance

Kurzfassung

Diese Diplomarbeit beschäftigt sich mit Näherungssensoren für die Erkennung und Lokalisierung von Objekten innerhalb eines Robotergreifers. Sogenannte berührungslose Sensorsystems schließen die Lücke zwischen bildgestützten (lange Distanz) und berührungsbasierten (kurze Distanz) Sensorsystemen für Anwendungen im Robotikbereich. Berührungslose Systeme können unterstützend für diverse Anwendungen in der Robotik verwendet werden, zum Beispiel beim Greifen von Objekten. Mit dem entwickelten berührungslosen Sensorsystem können stabförmige Objekte unterschiedlicher Materialien abhängig von der relativen Permittivität und Permeabilität erkannt und lokalisiert werden. In dieser Arbeit werden zwei verschiedene Messprinzipien untersucht und in Kombination eingesetzt, um die Anzahl der erkennbaren Objekte zu erhöhen. Der erste Teil des Sensorsystems macht sich den GMR-Effekt zu Nutze, um ferromagnetische Objekte zu detektieren. Zur Positionsbestimmung wird die Maximum-Likelihood-Methode eingesetzt. Der zweite Teil des Sensorsystems basiert auf der elektrischen Kapazitätstomographie, die es ermöglicht, Objekte an Hand ihrer relativen Permittivität zu erkennen und zu lokalisieren. Zwei Rekonstruktionsalgorithmen, ein deterministischer und ein statistischer, werden verwendet und ihre Ergebnisse verglichen. Der entwickelte Prototyp besteht aus zwei getrennten Teilen und ist dadurch sehr flexibel einsetzbar. Der erste Teil, bestehend aus den Sensoren und der Messdatenaufnahme, wird direkt am Robotergreifer montiert. Der zweite Teil besteht aus einer Empfangsstation und einem PC, welcher die Rekonstruktion ausführt. Der Datenaustausch zwischen den beiden Einzelkomponenten findet drahtlos über eine Funkverbindung statt. Die Anwendbarkeit dieses Ansatzes für das berührungslose Sensorsystem wird durch die gezeigten Rekonstruktionsergebnisse für stabförmige Objekte bestätigt.

Schlagwörter: Berührungloses Sensor System, Greifer, Objekt Lokalisierung, Maximum-Likelihood Methode, elektrische Kapazitätstomographie, GMR-Effekt

Contents

Chapter 1

Introduction

In the last decades autonomous robots have become more and more important not only in industrial applications but also in the field of unfamiliar environments, e.g., disaster rescue or domestic environments. Autonomous service robots supporting humans at home will become an essential part of our future daily live. Research initiatives have been founded to investigate the environmental needs for such robots. An example is the RoboCup @Home league of the RoboCup research initiative fostering research in the field of service robots, e.g., human-robot interaction, object manipulation, object recognition, etc. in domestic environments [Rob].

Object manipulation and grasping by a robot require a wide variety of sensors. Enabling these robotic systems to gather information about their environment in the same way humans do looks straightforward. Therefore, the most important senses for humans and robots are the eyes and vision, respectively.

Reliable grasping is very important for object manipulation in the field of robotics. Therefore, gathering sufficient information about an object's properties, e.g., material or shape, is essential for finding an optimal grasping point for an object. In the past, vision-based grasping planning strategies have shown good performances. However, the uncertainty in the object localization is leading to grasp failures (see [SDN08]).

The human abilities for object manipulation and grasping are not limited to their eyes. Humans also use the touch sense to gather additional information about an object, e.g., temperature, surface properties, hardness, weight and density. Trying to mimic the human sense of touch - tactile sensor systems are developed for grasper.

Tactile sensor systems can support vision-based systems to improve grasping, e.g., measuring contact force and slip (see [CCK05]). However, tactile sensor systems require touching the object to gather spatial information for finding a better grasping point for the object.

Robotic systems can be equipped with additional sensing capabilities which go beyond the capabilities of humans. Such systems are a part of pretouch sensor systems.

Beside vision (long distance) and tactile sensor systems (short distance) pretouch sensor systems are closing the gap between those systems. A pretouch sensor system gives spatial information prior to touching the object. Therefore, it can be used to gather prior knowledge of an object's pose to improve the alignment of the gripper arm and grasper to enhance the reliability of grasping an object. Depending on the measurement principle pretouch sensors are suitable for object recognition and localization with respect to the material properties covering the area close to the grasper. Therefore, it can be used to aid vision and contact-based systems finding an optimal grasping point to improve the reliability of grasping and to support the object manipulation.

1.1 Problem Statement

The aim of this work is to develop a pretouch sensor system for a robotic grasper (parallel jaw gripper). The system should be able to recognize and localize a variety of objects based on their material properties, e.g., ferromagnetic objects, within the interior of the grasper (region of interest). For this purpose two sensor types, capacitance sensors and magnetic field sensors are examined.
The magnetic part is inspired by the magnetic field tomography where a static magnetic field is utilized in combination with giant magnetoresistance (GMR) sensors measuring the distortion of the magnetic field caused by the ferromagnetic object.
The capacitive sensing part uses a measurement principle measuring the capacitances between two electrodes at a time. The position estimation is inspired by the electrical capacitance tomography (ECT) and is based on the previous work done at the *Institute of Electrical Measurement and Measurement Signal Processing*, *Graz University of Technology*. Figure 1.1 depicts the components of the sensor system.
The research questions are:

> Is it possible to recognize and localize objects based on their material properties, i.e. relative permittivity and relative permeability, using this combination of magnetic and capacitive sensors?
> Is the ECT approach suitable for a grasper to obtain a reliable reconstruction of an object's position?

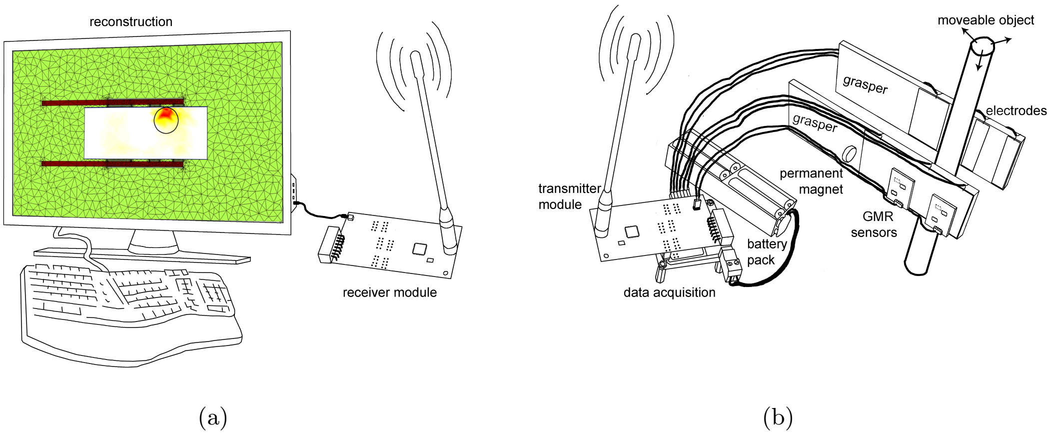

Figure 1.1: Overview of a pretouch sensor system for a robot grasper: example sketch comprising magnetic sensors, capacitive sensors, mobile unit and processing unit. (a) Stationary unit of the pretouch sensor system. (b) Mobile unit of the pretouch sensor system. The mobile unit is connected via a radio frequency link to the mobile unit.

1.2 Related Work

Recently developed pretouch sensor systems are based on optical proximity sensors (see Hasio et al. [HNH^{+}09]) and capacitive proximity sensors (see [SGWK07] and Mayton et al. [MGLS09]). Hsiao et al. describe an optical proximity system with twelve optical proximity sensors assembled inside a barrett hand, four on each finger tip. The sensor model uses three sensors arranged in a triangle to estimate the pose (distance and orientation) of the object's surface. While grasping, a reactive controller maintains the position of the fingers and the hand to the object. It ensures that the gripper arm centers the hand to the object and the fingers are at equal distance to the object's surface. The optical approach yielded good results for grasping a wide range of objects but is limited to the surface properties of the objects. Objects with highly reflective or transparent surfaces like a metallic can or a glass of water, respectively, could not be detected due to interferences.

The capacitive approach described by Mayton et al. distinguishes conductive and non-conductive objects with a different relative permittivity using pairwise transmitter and receiver electrodes. The sensing range depends on the distance between the transmitter and receiver electrodes. The electrodes are assembled inside the barrett hand covering three sensing ranges (short-, mid-, and long-term sensing). The different sensing ranges are utilized for the proportional integral derivate (PID) controllers of the arm and fingers to align the arm and hand with the object to be grasped. Mayton et al. demonstrated self pickup if the object is within a certain range and smooth human-robot object transfer.

It was shown that it is possible to detect if the object is touched by a human. Therefore, the object is released by the barrett hand if a person touches the object.
Comparing both systems, the optical proximity system has a greater variety of detectable objects. However, the described failure cases could easily be overcome by combining both sensor approaches and additionally the range of objects to be sensed could be extended.

This work is structured as follows: Chapter 2 describes the magnetic sensing approach including the simulation framework, the Gaussian process and the maximum likelihood estimator used to reconstruct the position of a ferromagnetic object. The electrical capacitance tomography including the two different reconstruction methods used to reconstruct objects based on their relative permittivity are presented in Chapter 3. The prototype of the pretouch sensor system is depicted in Chapter 4. In Chapter 5 the experimental results of the entire pretouch system are discussed. Finally, Chapter 6 presents the conclusion and ideas for possible future work. Appendix A contains all software-related components, e.g., configuration tool, prototype configuration, etc., and Appendix B presents the developed and used hardware for the prototype.

Chapter 2

Magnetic Sensing System

This chapter presents the magnetic sensing system of the pretouch sensor system. Section 2.1 contains the system description and theoretical background. The simulation framework used to solve the forward problem can be found in Section 2.2. The regression with Gaussian processes is described in Section 2.3. Sections 2.4 and 2.5 present the calibration method and the maximum likelihood estimator to calculate the position in the sensing domain Ω_{ROI} (region of interest). Finally, snapshots of the online reconstruction are shown in Section 2.6.

2.1 Theory and Measurement Principle

The reconstruction of the position of a ferromagnetic object using a permanent magnet and two magnetic field sensors measuring the field deviation is a classical inverse problem [NKK07]. The deviation is caused by the interaction of a ferromagnetic object with the magnetic field. The inverse problem arises due to the fact that the position is not a directly accessible variable although it can be determined from measurement data (magnetic field sensors) using a mathematical model. The magnetic field lines do not penetrate through obstacles in a straight way. In context of inverse problems this behavior is called a soft field problem [Bra07]. The mathematical model to solve the inverse problem in the problem domain Ω (and especially in the region of interest defined as Ω_{ROI}) can be described using Maxwell's equations for static magnetic fields.

Ampére's law is defined as follows: *"The line integral of* $\boldsymbol{H}$ *around a closed path is the same as the net current* $I_{enclosed}$ *enclosed by the path"* [Sad07]. In differential form this integral can be written as

$$\nabla \times \boldsymbol{H} = \boldsymbol{J}, \tag{2.1}$$

which is Maxwell's curl equation for static magnetic fields. $\boldsymbol{H}$ denotes the magnetic field intensity and $\boldsymbol{J}$ the current density. In our case

$$\nabla \times \boldsymbol{H} = 0, \tag{2.2}$$

due to fact that there are no electric currents. Because of $\nabla \times \boldsymbol{H} = 0$ the magnetic scalar potential Φ can be introduced as follows

$$\boldsymbol{H} = -\nabla \Phi. \tag{2.3}$$

The fourth Maxwell's equation describing the nonexistence of magnetic monopoles (no sources or sinks) is defined as

$$\nabla \cdot \boldsymbol{B} = 0. \tag{2.4}$$

Here, $\boldsymbol{B}$ denotes the magnetic flux density.

The constitutive relation between the magnetic flux density $\boldsymbol{B}$ and the magnetic field intensity $\boldsymbol{H}$ for the permanent magnet is

$$\boldsymbol{B} = \mu_0 \mu_r \boldsymbol{H} + \boldsymbol{B_r}. \tag{2.5}$$

$\boldsymbol{B_r}$ represents the remanent flux density. $\boldsymbol{B_r}$ is set to zero for the remainder problem domain Ω. The spatial magnetic material properties are μ_0 and μ_r denoting the permeability of free space and the relative permeability, respectively.

From the fourth Maxwell's equation 2.4 using equation 2.5 and 2.3 the elliptic partial differential equation (PDE) is obtained as follows

$$\begin{aligned} \nabla \cdot \boldsymbol{B} &= 0 \\ \nabla \cdot (\mu_0 \mu_r \boldsymbol{H} + \boldsymbol{B_r}) &= 0 \\ \nabla \cdot \mu_0 \mu_r (-\nabla \Phi) + \boldsymbol{B_r} &= 0 \\ -\nabla \cdot (\mu_0 \mu_r \nabla \Phi - \boldsymbol{B_r}) &= 0 \end{aligned} \tag{2.6}$$

This mathematical model shows the physical measurement principle and how a ferromagnetic object effects $\boldsymbol{B}$. Furthermore, the measurement process P can be defined as

$$P : \mu_r \mapsto \boldsymbol{B}(\boldsymbol{Z}) \tag{2.7}$$

Hence, the obtained measurement readings $\widetilde{\boldsymbol{d}}$ are a function of $\boldsymbol{B}(\boldsymbol{Z})$, where $\boldsymbol{Z}$ represents the measurement coordinates of Ω_{ROI}. In Section 6.1 an extension to the physical measurement problem is suggested for further improvements. Figure 2.1 depicts the necessary components of the measurement setup for the magnetic part of the pretouch sensor system. A permanent magnet and two magnetic field sensors are mounted on the backside of the grasper. A wide range of magnetic field sensors can be used, e.g., GMR sensors, which are discussed in the next section.

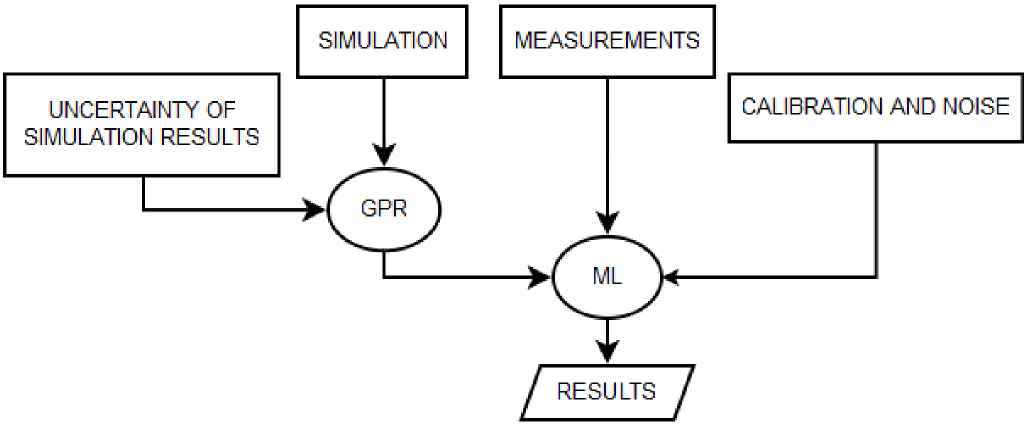

Figure 2.1: Block diagram of process steps resulting in a reconstruction result.

2.1.1 Giant Magnetoresistance Sensors

The phenomenon of magnetoresistance (MR) describes the interaction between the resistance of a conductor and an externally applied magnetic field, discovered by Thomson in 1856/57 [Tho57]. More than a century later in 1988 another milestone was achieved by the two scientists Peter Grünberg and Albert Fert. They independently discovered an artificial layer structure of ferromagnetic and non-magnetic metals (see Figure 2.2) with a huge MR named giant magnetoresistance (GMR) [Nob07].
The most essential part of a GMR sensor is its layer structure. Three different layer structures are commonly in use.

- The spin valve technology is a four-layer structure consisting of an anti-ferromagnetic layer, a pinned-ferromagnetic layer, a non-magnetic layer and a ferromagnetic layer which are stacked onto each other [FSO+00].
- Grünberg [GBZ89] developed a three-layer structure consisting of a non-magnetic metallic layer (nanometer thick) which is sandwiched by two ferromagnetic layers.
- Fert [BBF+88] developed a multi-layer structure consisting of a three-layer structure repeated several times.

Depending on the width of the non-magnetic interlayer(s) the electrons of the non-magnetic layer(s) provide the coupling between the two ferromagnetic layers. The magnetization of the ferromagnetic layers are antiparallel polarized as long as there is no external magnetic field applied and the resistance is high. In case of an external magnetic field the magnetization of the two layers becomes parallel. Therefore, the resistance varies due to the altered polarization of the two ferromagnetic layers. In this case (parallel polarization of both ferromagnetic layers) the resistance becomes small due to the change of the spin polarization of the ferromagnetic layer [Nob07]. The different layer structures are shown in Figure 2.2.

The variation of the resistance according to the applied magnetic field for GMR sensors from NVE [GMR] is shown in Figure 2.3(a). For this work two different GMR sensors with multi-layer structure from NVE are used. The AA006-02 from the AA series will be referred to GMR 2 and AAL002-02 from the AAL series will be referred to GMR 1. The internal sensor layout is a Wheatstone bridge with two shielded GMR resistors. The remainder of the bridge is influenced by the magnetic field and causes a change of the bridge output. The advantages of these sensors are a high sensitivity, e.g., AAL002-02 3–4.2 mV/V-Oe and AA006-02 0.9–1.3 mV/V-Oe, a wide linear range of operation and a very low magnetic hysteresis (2 % AAL series). In addition, the GMR sensors are tiny and therefore suitable for this application. Further details about theses sensors can be found in the datasheet (see [GMR]).

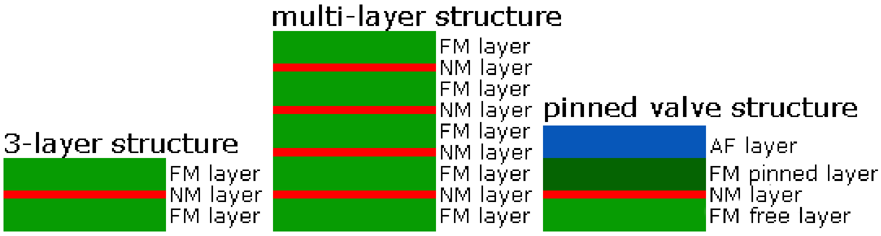

Figure 2.2: Layer structures of GMR sensors. FM denotes ferromagnetic, NM represents non-magnetic and AF denotes anti-ferromagnetic.

2.2 Simulation Framework

To solve the forward problem the physical measurement process P defined in Section 2.1 is simulated using a simulation framework. In this particular case the forward problem can be defined as: Given the position of the rod and using the mathematical model the values of the magnetic field intensity are obtained. In other words the forward map can be written as

$$F : \boldsymbol{\mu}_r \mapsto \boldsymbol{y} \tag{2.8}$$

to solve the forward problem. The vector $\boldsymbol{\mu_r}$ contains the discretization of μ_r and $\boldsymbol{y}$ represents the output of the forward map equates to the simulated magnetic sensor results.

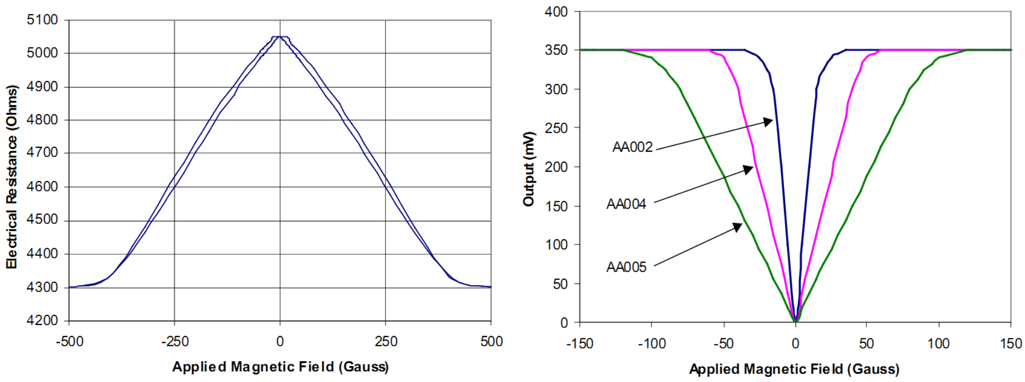

(a) (b)

Figure 2.3: (a) Resistance of NVE's multi-layer GMR material as a function of the applied magnetic field [GMR]. (b) Sensitivity of the series AA002, AA004 and AA005 with respect to the applied magnetic field [GMR].

The simulation uses the finite element method (FEM) to solve the equation 2.6 given the quantities $\boldsymbol{B_r}$ and $\boldsymbol{\mu_r}$. At the far boundary $\partial\Omega$ a so called magnetic insulation is applied within the simulation framework. The output $\boldsymbol{y}$ of the forward map F evaluated at two points (matching the true position of the GMR sensors of the real measurement setup) is used to feed the presented Gaussian process (GP) and the maximum likelihood estimate (MLE) in Sections 2.3 and 2.5. Therefore, the simulation must be executed for each position of an inclusion and is referred to as simulation sequence. This work is focused on rod-like inclusions in Ω_{ROI} whereas the position is defined as

$$\boldsymbol{x} = \begin{bmatrix} x & y \end{bmatrix}^T . \tag{2.9}$$

It should be noted that $\boldsymbol{x}$ is used in the entire work except in Section 2.3. The forward map F uses $\boldsymbol{x}$ as input to solve the forward problem. The simulation sequence is performed twice to avoid a discretization error which arises due to the remeshing of the problem domain Ω while the rod is moved within Ω_{ROI}. First, the simulation sequence is done setting $\mu_{\mathrm{r}} = 1$ and second the simulation is done using the relative permeability μ_r of the used material.

As simulation framework COMSOL Multiphysics was used to solve the forward problem as described above. Figure 2.4 depicts the grasper model within COMSOL Multiphysics. Detailed information about the simulation configuration of each simulation can be found in the file *readmeSimulationDescriptions.txt* of the software package. As shown in Figure 2.4 the simulation framework uses a 3D model. Therefore, the solution of the forward problem is associated with high computational effort. However, the forward problem has

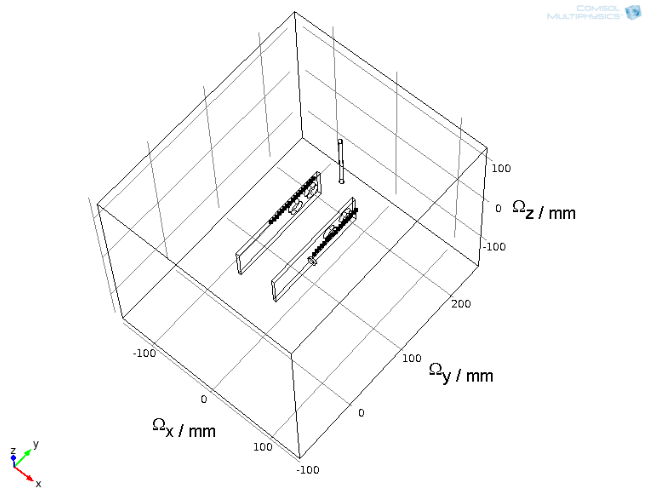

Figure 2.4: Simulation model used to obtain the simulation data.

to be solved only once which can be done in advance and subsequently used for the entire reconstruction process. Thus, the high computational effort does not affect the online reconstruction.

2.3 Gaussian Process

As shown in Figure 2.1 the MLE needs the data generated by the simulation framework to perform the position estimation of the object in Ω_{ROI}. However, the finite element method solving the forward problem as described above requires significant computational effort. Therefore, it looks straightforward to use a predictor to approximate the values between the supporting points (output of the simulation framework) to refine the data set used for the reconstruction. One advantage of this is that it increases the resolution of the position estimate done with the MLE. To solve the prediction problem it was decided to use a GP for regression because the GP provides uncertainty information.

Following the notation of Rasmussen (see [RW06]) a GP is denoted by both its mean function and covariance function

$$f(\boldsymbol{x}) \sim \mathcal{GP}\left(m(\boldsymbol{x}), k(\boldsymbol{x}, \boldsymbol{x}')\right). \tag{2.10}$$

It should be noted that $\boldsymbol{x}$ used in this section is different from the position $\boldsymbol{x}$ defined in the previous section (equation 2.9). Here,

$$\begin{aligned} m(\boldsymbol{x}) &= \mathcal{E}\left[f(\boldsymbol{x})\right] \\ k(\boldsymbol{x}, \boldsymbol{x}') &= \mathcal{E}\left[\left(f(\boldsymbol{x}) - m(\boldsymbol{x})\right)\left(f(\boldsymbol{x}') - m(\boldsymbol{x}')\right)\right] \end{aligned} \tag{2.11}$$

represents the mean function and the covariance function. For further calculations the mean function is set to zero as stated in [RW06].

A remarkable approach of the GP is the representation of the relation between the model input $\boldsymbol{x}$ and the model output $\boldsymbol{y}$ in form of a multivariate Gaussian distribution

$$\begin{bmatrix} \boldsymbol{y} \\ \boldsymbol{y}^* \end{bmatrix} = \mathcal{N}\left(\mathbf{0}, \begin{bmatrix} \boldsymbol{K}(\boldsymbol{x},\boldsymbol{x}) & \boldsymbol{K}(\boldsymbol{x},\boldsymbol{x}^*) \\ \boldsymbol{K}(\boldsymbol{x}^*,\boldsymbol{x}) & \boldsymbol{K}(\boldsymbol{x}^*,\boldsymbol{x}^*) \end{bmatrix}\right). \tag{2.12}$$

Here, $\boldsymbol{y}$ and $\boldsymbol{y}^*$ denote the training data and test data to predict. $\boldsymbol{x}$ and $\boldsymbol{x}^*$ represent the input of the training data and test data, respectively. From this the conditional distribution can be derived (see [RW06])

$$\boldsymbol{y^*}|\boldsymbol{y} \sim \mathcal{N}(\boldsymbol{K}(\boldsymbol{x}^*,\boldsymbol{x})\boldsymbol{K}(\boldsymbol{x},\boldsymbol{x})^{-1}\boldsymbol{y}, \boldsymbol{K}(\boldsymbol{x}^*,\boldsymbol{x}^*) - \boldsymbol{K}(\boldsymbol{x}^*,\boldsymbol{x})\boldsymbol{K}(\boldsymbol{x},\boldsymbol{x})^{-1}\boldsymbol{K}(\boldsymbol{x},\boldsymbol{x}^*)). \tag{2.13}$$

This leads to the prediction

$$\boldsymbol{y}^* = \boldsymbol{K}(\boldsymbol{x}^*,\boldsymbol{x})\boldsymbol{K}(\boldsymbol{x},\boldsymbol{x})^{-1}\boldsymbol{y} \tag{2.14}$$

and the corresponding variance can be written as

$$\operatorname{var}(\boldsymbol{y}^*) = \boldsymbol{K}(\boldsymbol{x}^*,\boldsymbol{x}^*) - \boldsymbol{K}(\boldsymbol{x}^*,\boldsymbol{x})\boldsymbol{K}(\boldsymbol{x},\boldsymbol{x})^{-1}\boldsymbol{K}(\boldsymbol{x},\boldsymbol{x}^*). \tag{2.15}$$

Further details about the covariance function $\boldsymbol{K}$ can be found in [RW06].

The results of the approximation and the according variance using the GP are shown in Figures 2.5 and 2.6 for GMR 1 and GMR 2, respectively. The output of the forward model depicted as blue pins in Figure 2.5(a) is the model input (training data) of the GP. The smooth surface is the predicted output of the GP which is further processed as input data for the MLE. The variance of the GP output is shown in Figure 2.5(b) for GMR 1.

2.4 Calibration Method

The raw GPR data and measurement data cannot be used as input of the MLE as shown in Figure 2.1. The position reconstruction of an inclusion will not work due to data mismatch. Therefore, an offset-gain calibration scheme is introduced to overcome this issue and to weaken the influence of the model errors. The measurement data of GMR1 and GMR2 is defined as

$$\widetilde{\boldsymbol{d}} = \begin{bmatrix} \widetilde{d}_{\mathrm{GMR1}} & \widetilde{d}_{\mathrm{GMR2}} \end{bmatrix}. \tag{2.16}$$

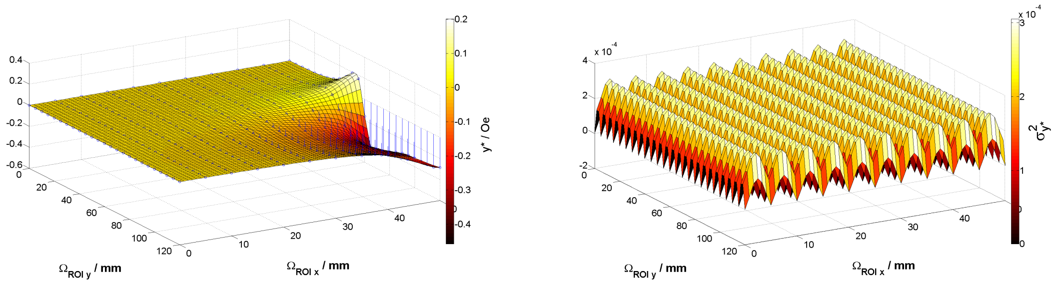

(a) (b)

Figure 2.5: Behavior of the Gaussian process model for GMR 1 sensor. (a) Estimated value $\boldsymbol{y}^*$. (b) Predicted variance $\sigma^2_{\boldsymbol{y}^*}$.

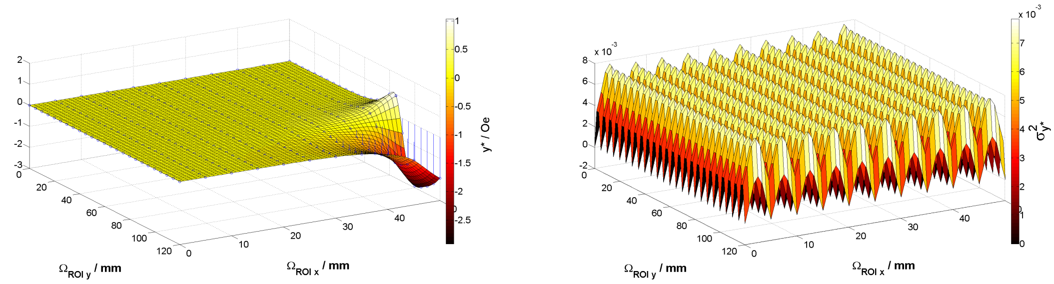

(a) (b)

Figure 2.6: Behavior of the Gaussian process model for GMR 2 sensor. (a) Estimated value $\boldsymbol{y}^*$. (b) Predicted variance $\sigma^2_{\boldsymbol{y}^*}$.

The following equation represents the offset-gain calibration for a single element of the measurement data $\widetilde{\boldsymbol{d}}$

$$\tilde{d}_c = y_{\text{air}} + \underbrace{\frac{y_{\text{rod}} - y_{\text{air}}}{d_{\text{rod}} - d_{\text{air}}}}_{k} \left(\tilde{d} - d_{\text{air}}\right), \tag{2.17}$$

where the indices rod and air denote the results of the GPR and measurement with a steel rod at the calibration position and the absence of an object within Ω_{ROI} (empty Ω_{ROI}). Here, k denotes the gain correction factor between the simulation model and the real model. As seen in equation 2.17, k is a function of the calibration position of a rod and can be treated as a random variable introducing an additional error which should be addressed. This looks like a drawback since the reconstruction will not work properly without the offset-gain calibration. This issue is considered in the covariance Matrix $\boldsymbol{C}$ of the MLE in equation 2.22. After the offset-gain calibration, $\tilde{\boldsymbol{d}}_{\boldsymbol{c}}$ is used for further processing in the upcoming section.

The calibration position for one exemplary sensor is defined as $\boldsymbol{x}_{cal\ pos} = [\Omega_{\text{ROI x}}\ \Omega_{\text{ROI y}}]$.

Currently, the implemented calibration positions for GMR 1 and GMR 2 are $\Omega_{\text{roi y}} = 90\,\text{mm}$, $\Omega_{\text{roi x}} = 35\,\text{mm}$ and $\Omega_{\text{roi y}} = 70\,\text{mm}$, $\Omega_{\text{roi x}} = 40\,\text{mm}$, respectively. It should be noted that the calibration position of a steel rod 3 mm in radius, placed perpendicular to the plane spanned by Ω_{ROI}, is at the top center of the circle (seen from top view of the rod). This calibration was applied to all presented measurement results of Section 2.6 and Chapter 5.

2.5 Maximum Likelihood Estimator

The MLE is a practical estimator which can be used for sophisticated estimation problems. In this work the MLE is used to estimate the position $\boldsymbol{x}$ of a rod-like inclusion in Ω_{ROI}. The MLE has several favorable properties, e.g., it has an asymptotically normal distribution, it is asymptotically efficient and is asymptotically optimal as stated in [Kay93] (Theorem 7.1). These asymptotic properties hold true only if the data set is large enough. Beside the asymptotic properties another tremendous advantage of the MLE is that it can always be found numerically for a given finite data set because it is the maximum of the likelihood function (defined in equation 2.20). Therefore, it is not necessary to implement an iterative maximization method, e.g., Newton-Raphson or method of scoring. In this work the MLE is determined numerically by applying a grid search method which is feasible due to the finite data set Ω_{ROI}. It should be noted that this grid search has to be repeated every time new measurement data is received (see [Kay93]).

In general, the MLE of a differentiable likelihood function can be computed by

$$\frac{\partial \ln p\left(\widetilde{\boldsymbol{d}}_{\boldsymbol{c}};\boldsymbol{x}\right)}{\partial \boldsymbol{x}} = 0 \tag{2.18}$$

given the linear model

$$\widetilde{\boldsymbol{d}}_{\boldsymbol{c}} = \boldsymbol{x} + w. \tag{2.19}$$

Here, w is a noise vector with the probability density function (PDF) $\mathcal{N}(0;\boldsymbol{C})$. Therefore, the log-likelihood function to determine the probability of the rod's position in Ω_{ROI} given the GPR data (simulation data) and measurement data can be written as

$$p\left(\widetilde{\boldsymbol{d}}_{\boldsymbol{c}};\boldsymbol{x}\right) = \log\left(\frac{1}{(2\pi)^{\frac{N}{2}}\,|\boldsymbol{C}|^{\frac{1}{2}}}\exp\left(-\frac{1}{2}\boldsymbol{e}^T\boldsymbol{C}^{-1}\boldsymbol{e}\right)\right), \tag{2.20}$$

Here, N denotes the number of used GMR sensors (measurement signals). $\boldsymbol{e}$ expresses the error vector

$$\boldsymbol{e}(\boldsymbol{x}) = \boldsymbol{y}(\boldsymbol{x}) - \widetilde{\boldsymbol{d}}_{\boldsymbol{c}} \tag{2.21}$$

and $\boldsymbol{C}$ denotes the covariance function as defined by

$$\boldsymbol{C} = \begin{bmatrix} \Delta h_1^2 & 0 \\ 0 & \Delta h_2^2 \end{bmatrix} + \sigma_n^2 \boldsymbol{I} + \sigma_{\text{model}}^2 \boldsymbol{I}. \tag{2.22}$$

The covariance function holds only entries in the main diagonal due to statistical independence of the measurement data. The first term addresses the known hysteresis of 4 % (see [GMR]) of both GMR sensors. The second term implies the measurement noise with variance σ_{n}^2, where $\boldsymbol{I}$ denotes the identity matrix. Finally, the uncertainty of the model σ_{model}^2 occurring due to model assumptions and the predicted variance $\sigma_{\boldsymbol{y}^*}^2$ of the GPR can be used. The correlated errors caused by an inaccurate positioning of the magnet are to a large extent addressed by the used calibration method.
The MLE is the maximum of the log-likelihood function representing the estimated position and can be obtained by maximization of equation 2.20 as follows

$$\widetilde{\boldsymbol{x}} = \arg\max \left\{ p\left(\widetilde{\boldsymbol{d}}_{\boldsymbol{c}}; \boldsymbol{x} \right) \right\}. \tag{2.23}$$

An online reconstruction using the described MLE from above is implemented in MATLAB. Selected snapshots of the online reconstruction are presented in the next section. For further information about the MLE see [Kay93].

2.6 Results

This section shows the online reconstruction results for rod-like inclusions in Ω_{ROI} of the presented magnetic sensing system.

Figures 2.7(a) to 2.10(a) show the measurement signals of the two GMR sensors for a steel rod, 3 mm in radius, moved from the left to the right at a certain distance to the grasper. The corresponding snapshots of the online reconstructions which are the outputs of the MLE (compare equation 2.23) are shown in Figures 2.7(b) to 2.10(b). The maximum of the log-likelihood and the true position of the steel rod have a close match. The reconstruction results show that it is possible to recognize objects based on their relative permeability and to determine the position of a rod. However, due to the soft field properties, it is not possible to draw conclusions about the shape or radius of a rod.

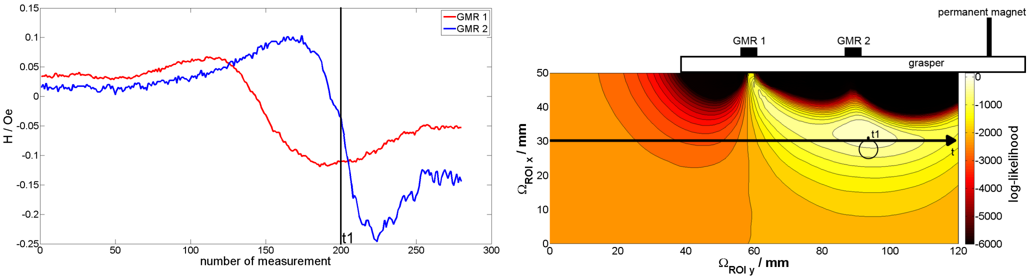

(a) (b)

Figure 2.7: Measurement signal and corresponding reconstruction result. (a) Obtained sensor signal after offset-gain calibration where a steel rod was moved along the y-axis (from $0 - 120\,\text{mm}$) at $x = 30\,\text{mm}$. At time t1 both measurement signals of the GMR sensors are unique. Therefore, a reconstruction of the position is possible. (b) Snapshot of the online reconstruction of Ω_{ROI} while the rod is moved along the y-axis at time t1. The black circle depicts the true position of the rod at $x = 30\,\text{mm}$ and $y = 95\,\text{mm}$. The maximum of the log-likelihood (color bar) is the MLE. The color shades show how likely it is for an object to be positioned at a certain place. The MLE and the true position of the steel rod (top center of the black circle) have a close match.

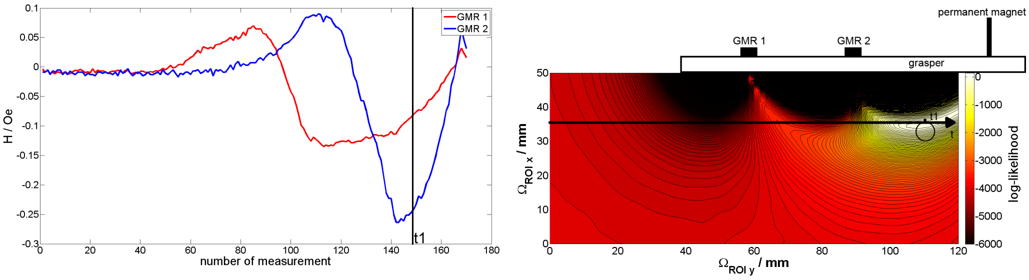

(a) (b)

Figure 2.8: Measurement signal and corresponding reconstruction result. (a) Obtained sensor signal after offset-gain calibration where a steel rod was moved along the y-axis (from $0 - 120\,\text{mm}$) at $x = 35\,\text{mm}$. At time t1 both measurement signals of the GMR sensors are unique. Therefore, a reconstruction of the position is possible. (b) Snapshot of the online reconstruction of Ω_{ROI} while the rod is moved along the y-axis at time t1. The black circle depicts the true position of the rod at $x = 35\,\text{mm}$ and $y = 115\,\text{mm}$. The maximum of the log-likelihood (color bar) is the MLE. The color shades show how likely it is for an object to be positioned at a certain place. The MLE and the true position of the steel rod (top center of the black circle) have a close match.

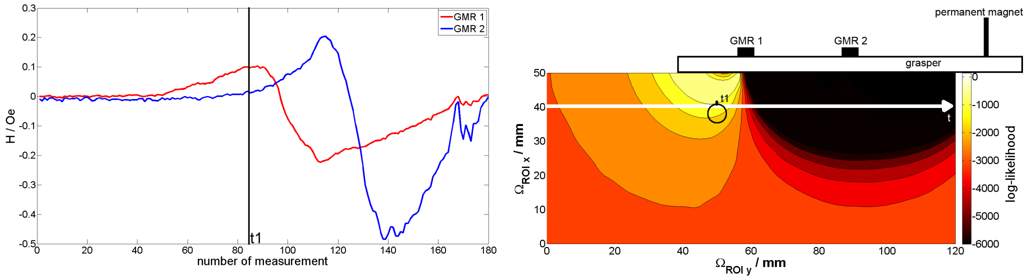

(a) (b)

Figure 2.9: Measurement signal and corresponding reconstruction result. (a) Obtained sensor signal after offset-gain calibration where a steel rod was moved along the y-axis (from $0 - 120\,\text{mm}$) at $x = 40\,\text{mm}$. At time t1 both measurement signals of the GMR sensors are unique. Therefore, a reconstruction of the position is possible. (b) Snapshot of the online reconstruction of Ω_{ROI} while the rod is moved along the y-axis at time t1. The black circle depicts the true position of the rod at $x = 40\,\text{mm}$ and $y = 50\,\text{mm}$. The maximum of the log-likelihood (color bar) is the MLE. The color shades show how likely it is for an object to be positioned at a certain place. The MLE and the true position of the steel rod (top center of the black circle) have a close match.

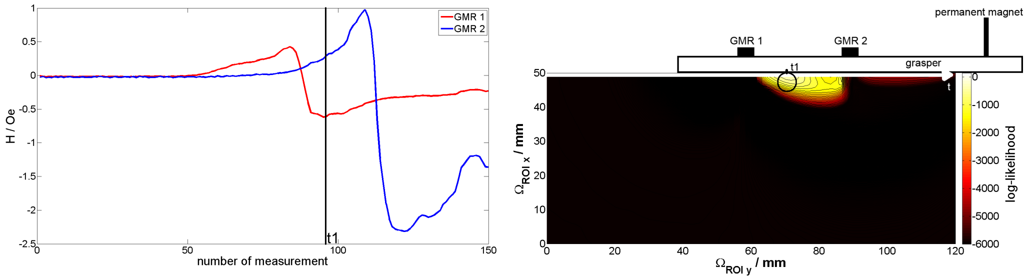

(a) (b)

Figure 2.10: Measurement signal and corresponding reconstruction result. (a) Obtained sensor signal after offset-gain calibration where a steel rod was moved along the y-axis (from $0 - 120\,\text{mm}$) at $x = 50\,\text{mm}$. At time t1 both measurement signals of the GMR sensors are unique. Therefore, a reconstruction of the position is possible. (b) Snapshot of the online reconstruction of Ω_{ROI} while the rod is moved along the y-axis at time t1. The black circle depicts the true position of the rod at $x = 50\,\text{mm}$ and $y = 70\,\text{mm}$. The maximum of the log-likelihood (color bar) is the MLE. The color shades show how likely it is for an object to be positioned at a certain place. The MLE and the true position of the steel rod (top center of the black circle) have a close match.

Figure 2.11 compares the reconstruction results for rods different in radius from the rod used for the forward problem. It clearly shows that the prediction of the positions for the two rods are not accurate anymore. Therefore, this measurement setup is limited to the reconstruction of the position of rod-like inclusions with 3 mm in radius. For the reconstruction of other inclusions this measurement setup must be extended and further simulations have to be done as described in Section 6.1.

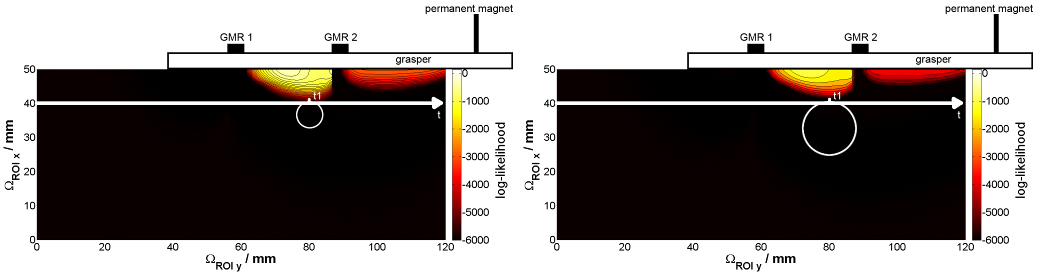

(a) (b)

Figure 2.11: Reconstruction results for rods different in radius at position x = 40 mm and y = 80 mm in both cases. The white circles depict the positions of the rods. The maximum of the log-likelihood (color bar) is the MLE. The color shades show how likely it is for an object to be positioned at a certain place. (a) Radius of the steel rod is 4 mm. The MLE and the true position of the steel rod (top center of the white circle) do not match. (b) Radius of the steel rod is 8 mm. The MLE and the true position of the steel rod (top center of the white circle) do not match.

Figure 2.12 shows the sensing range of the magnetic sensing system in detail. Two snapshots of the online reconstruction with no inclusion and a steel rod (radius: 3 mm) in Ω_{ROI} are presented in comparison. Shown in Figure 2.12(a) the sensor range is split up into three zones. This is due to the high gradient of the sensor signal at the moment of zero passing as shown in Figures 2.5 and 2.6. Due to the sensor arrangement and the decreasing magnetic field the sensor signal decreases along the y-axis (from right to left) and along the x-axis (from top to bottom). The achieved sensor measurement range is 20 mm along the x-axis and 80 mm along the y-axis. Therefore, the best localization can be obtained at the top center and top right of Ω_{ROI}. To overcome these limitations the sensor range can be augmented, e.g., by using additional GMR sensors and additional electro magnets instead of one single permanent magnet as suggested in Section 6.1. A ferromagnetic object placed outside the sensing range cannot be reconstructed and localized as shown in Figure 2.12(b).

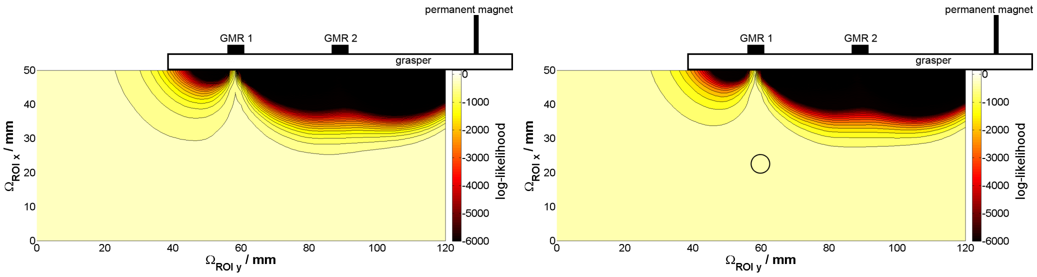

(a)

(b)

Figure 2.12: Sensing range of the magnetic sensing system. (a) Snapshot of the online reconstruction of Ω_{ROI} with no inclusion. The maximum of the log-likelihood (color bar) is the MLE. The color shades show how likely it is for an object to be positioned at a certain place. In this case the MLE covers three quarters of Ω_{ROI}. (b) Snapshot of the online reconstruction of Ω_{ROI} with a steel rod. The black circle depicts the true position of the rod at $x = 25\,\mathrm{mm}$ and $y = 60\,\mathrm{mm}$. In this case the object cannot be localized because the object is placed outside the sensing range of the magnetic sensing system. In comparison to (a) the steel rod does not influence the log-likelihood and the MLE covers the same area.

Chapter 3

Electrical Capacitance Tomography

In this chapter the capacitive part of the pretouch sensor system is presented. First, a short introduction to electrical capacitance tomography (ECT) is given. Section 3.1 describes the theoretical background and the measurement principles of the ECT. The definition of the inverse problem is stated in the Section 3.2. Details about the used calibration method can be found in Section 3.3. The used reconstruction methods are presented in Section 3.4. Finally, the reconstruction results for both reconstruction methods are shown at the end of this chapter in Section 3.5.

Within ECT, electrodes are arranged around the region of interest (ROI) measuring the capacitance between them. From these measurements the spatial permittivity distribution is obtained by the solution of the inverse problem. ECT is a non-invasive method commonly used for industrial processes measuring, e.g., for multi-phase flows like oil and water in pipes. This can be done easily due to the clear diversity of the materials' permittivity. The ECT can be used for 2-D and 3-D permittivity distribution determination of a cross-sectional area or volume of a pipe. The application domains include, but are not limited to borehole measurements, imaging material structures, food quality and food safety [Bra07].

Starting in 2002, the model based measurement group at the *Institute of Electrical Measurement and Measurement Signal Processing* at *Graz University of Technology* developed an ECT prototype system [Weg06] for multi-phase flows to determine the permittivity distribution inside a closed pipe. The ongoing progress and improvement of the reconstruction algorithm led to an improvement of the reconstruction speed and accuracy.

This work investigates if the framework is suitable to determine the permittivity distribution in the interior of a robot grasper. The fundamental question is whether a reliable reconstruction of an object position is possible using fewer electrodes and a different geometry. Therefore, the existing framework and the latest reconstruction algorithms to speed up the reconstruction time from [Neu11] were adapted to make them applicable for a robot grasper (parallel jaw gripper) as described later in Section 3.4. Figure 3.1 shows the electrode arrangement and associated capacitances between them.

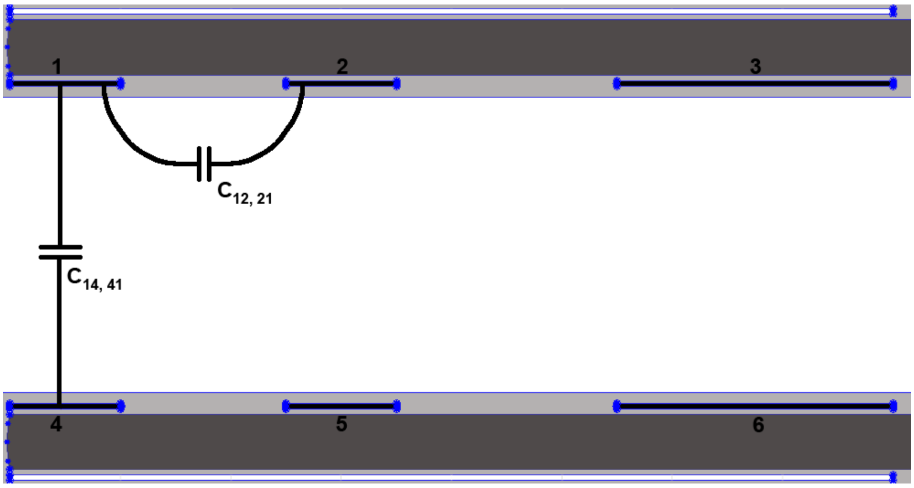

Figure 3.1: ECT measurement principle. The black, white, dark and light gray colors depict the electrodes, ROI, grasper and surrounding area. Two of the 15 measured capacitances, i.e. $C_{12,21}$ and $C_{14,41}$, are shown exemplarily.

3.1 Theory and Measurement Principle

Gauss's law is defined as follows: *"The total electric flux Ψ through any closed surface is equal to the total charge enclosed by that surface"* [Sad07]. The integral and differential form of Maxwell's equation can be written as

$$\begin{aligned} Q = \oint_S \boldsymbol{D} \cdot d\boldsymbol{S} = \int_\nu \rho_\nu d\nu, \text{ and} \\ \nabla \cdot \boldsymbol{D} = \rho_\nu. \end{aligned} \tag{3.1}$$

Where Q is the total charge enclosed, $\boldsymbol{S}$ denotes the surface, $\boldsymbol{D}$ is the electric flux density and ρ_ν expresses the volume charge density. Next, the electric flux density $\boldsymbol{D}$ can be written as

$$\boldsymbol{D} = \varepsilon_0 \varepsilon_r \boldsymbol{E} \tag{3.2}$$

where ε_0 and ε_r denote the permittivity of free space and the relative permittivity, also written as $\varepsilon = \varepsilon_0\varepsilon_r$. The electric field is expressed by $\boldsymbol{E}$.

The charge Q and the capacitances C are linked by the relation

$$Q = CV_0 \tag{3.3}$$

where V denotes the electric potential.

The electric potential difference along a closed path must be zero. Applying Stokes's theorem to this statement the curl of the electric field can be derived as follows [Sad07]

$$\begin{aligned} \oint_L \boldsymbol{E} \cdot d\boldsymbol{l} &= 0 \\ \oint_L \boldsymbol{E} \cdot d\boldsymbol{l} &= \int_S (\nabla \times \boldsymbol{E}) \cdot d\boldsymbol{S} = 0 \end{aligned} \tag{3.4}$$

implying that

$$\nabla \times \boldsymbol{E} = 0. \tag{3.5}$$

The definition of the electric potential can be rewritten to

$$\begin{aligned} V =& -\int \boldsymbol{E} \cdot d\boldsymbol{l} \\ dV =& -E_x dx - E_y dy - E_z dz. \end{aligned} \tag{3.6}$$

Moreover, a total charge can be expressed by the sum of its partial charges as

$$\begin{aligned} dV &= \frac{\partial V}{\partial x} dx + \frac{\partial V}{\partial y} dy + \frac{\partial V}{\partial z} dz \\ E_x &= -\frac{\partial V}{\partial x},\ E_y = -\frac{\partial V}{\partial y},\ E_z = -\frac{\partial V}{\partial z} \end{aligned} \tag{3.7}$$

Thus, the electric field $\boldsymbol{E}$ is the gradient of the electric potential V

$$\boldsymbol{E} = -\nabla V \tag{3.8}$$

implicitly satisfying the identity $\nabla \times (\nabla V) = 0$ for equation 3.5 [Sad07].

Using the differential form of Gauss's law 3.1 and the equations 3.2 and 3.8, the partial differential equation describing the electrical field problem in the domain Ω can be obtained as shown below

$$\begin{aligned} \nabla \cdot \boldsymbol{D} = \rho_\nu &= 0 \\ \nabla \cdot (\varepsilon_0 \varepsilon_r \boldsymbol{E}) &= 0 \\ \nabla \cdot (\varepsilon_0 \varepsilon_r (-\nabla V)) &= 0 \end{aligned} \tag{3.9}$$

Rewriting equation 3.3 and using Gauss's law from equation 3.1 in combination with the relations given in equations 3.2 and 3.8, the capacitances can be calculated as follows

$$\begin{aligned}C &= \frac{Q}{V_0} \\ C &= \frac{1}{V_0}\oint_S \boldsymbol{D}\cdot d\boldsymbol{S} \\ C &= \frac{1}{V_0}\oint_S \varepsilon_0\varepsilon_r \boldsymbol{E}\cdot d\boldsymbol{S} \\ C &= -\frac{1}{V_0}\oint_S \varepsilon_0\varepsilon_r \nabla V d\boldsymbol{S}.\end{aligned} \tag{3.10}$$

Taking into account the following Dirichlet type boundary conditions on $\partial\Omega$ (boarder of problem domain Ω) and on the electrodes

$$\begin{aligned}V_{S_{Tx}} &= V_0 \\ V_{S_{Rx}} &= 0 \\ V_{\partial\Omega} &= 0 \text{ [NZWF11].}\end{aligned} \tag{3.11}$$

3.1.1 AD7746

Figure 3.2 illustrates the measurement principle of the 24-bit capacitance to digital converter (CDC) AD7746 from Analog Device. The capacitance is measured between a transmitter electrode (Tx) and a receiver electrode (Rx). Therefore, an alternate current (AC) excitation signal is excited to the transmitter electrode. The capacitance between both electrodes is influenced by objects within the sensing range depending on their dielectric properties. It should be noted that the AD7746 was used for all presented measurement results.

3.1.2 AD7148

In comparison to AD7746 the AD7148 has a different capacitive sensing principle as illustrated in Figure 3.3(a) and a lower resolution of 16-bit. The AD7148 measures the capacitance between a single electrode and the ground. Therefore, the transmitter electrode connected to AD7148 is applied with a square wave excitation signal. The object acts as receiving electrode forming the capacitor with the electrode connected to the sensing chip. As already mentioned in the previous section the influence depends on the dielectric properties of the object. To minimize the influence of stray capacitances, the AD7148 has an AC_{SHIELD} pin which should be used between the transmitter electrode and the sensor chip package as illustrated in Figure 3.3(b).

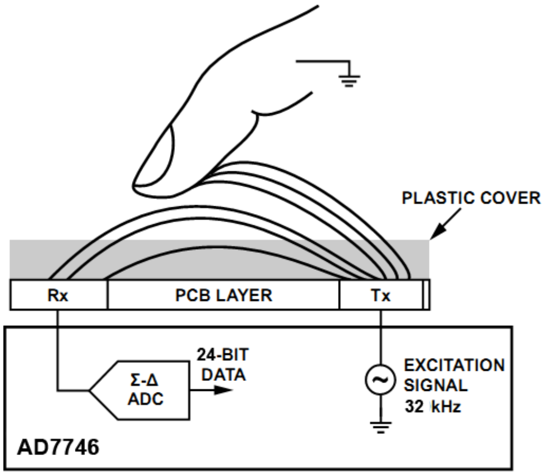

Figure 3.2: Capacitance measuring principle of AD7746 [Ana05]. It should be noted that within ECT the approaching object is not grounded.

The measurement data of both sensing chips (AD7746 and AD7148) is read out via the I2C [NXP07] interface as described in the data sheets [Ana10] and [Ana10].

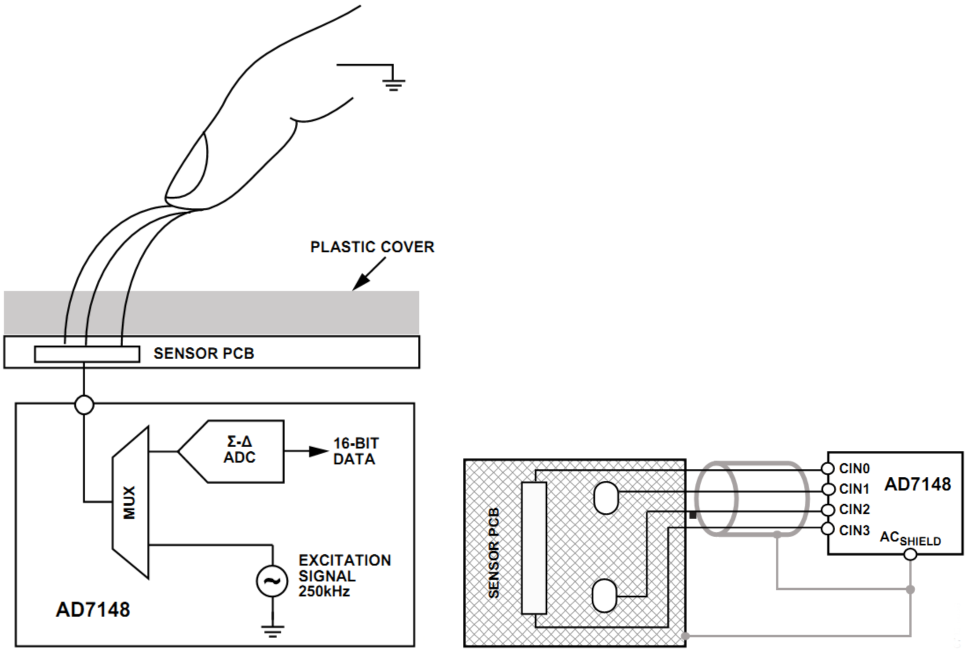

(a) (b)

Figure 3.3: (a) Capacitance measuring principle of AD7148. It should be noted that within ECT the approaching object is not grounded. [Ana10]. (b) Recommended AC_{SHIELD} configuration [Ana10].

3.2 Inverse Problem

As already mentioned in the introduction of this chapter, ECT is a problem of inverse nature. As in the case of the magnetic sensing system the ECT is a so-called soft field inverse problem due to the bending of the field lines [Bra07]. Another important criterion to solve an inverse problem was defined by Hadamard [Had02] in 1902. A problem is well posed if the following requirement is fulfilled

- A unique solution, continuously depending on the data, exists.

However, in the particular case of the ECT this requirement is not met. Therefore, the ECT is defined as an ill-posed inverse problem and needs a regularization to obtain a feasible solution.

The forward map for the ECT can be formally written as

$$F : \boldsymbol{\varepsilon} \mapsto \boldsymbol{C} \tag{3.12}$$

to solve the forward problem. $\boldsymbol{\varepsilon}$ contains the discretization of the permittivity and the output of the forward problem is the determined capacitance matrix $\boldsymbol{C}$. To solve the forward problem the FEM is used. Figure 3.4 depicts the FE structure of the entire problem domain Ω.

To determine the charges the forward problem must be solved. Therefore, a variety of methods can be used, e.g., the charge method or the charge integration. In this work, an approach with the Green's functions as described and implemented by [NF10] to solve the forward problem is used. Using Green's functions the charges can be calculated as follows

$$\boldsymbol{Q} = \boldsymbol{Q}_a + \boldsymbol{G}_Q^T \boldsymbol{R}. \tag{3.13}$$

Here, $\boldsymbol{G}_Q^T$ and $\boldsymbol{Q}_a$ denote the Green's functions and the affine charges (from the back side capacitances), respectively. Solving the forward problem using the Green's functions requires the same computational effort as using the other methods such as the charge method. However, the big advantage of the Green's functions is to calculate the product of the transpose of Jacobian matrix and the residual $\boldsymbol{J}^T \boldsymbol{r}_k$ needed to solve the inverse problem for both reconstruction methods described in Section 3.4. The Jacobian matrix contains the derivatives of the charges with respect to the permittivity values. For further details about using the Green's functions and derivations to solve the forward problem and to calculate the Jacobian see [NF10].

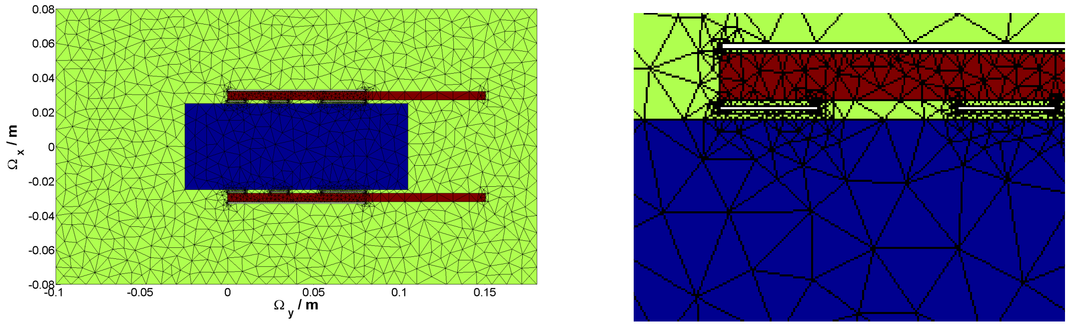

(a) (b)

Figure 3.4: Discretization of the problem domain Ω to solve the forward problem. (a) The red color depicts the grasper, the region of interest Ω_{ROI} is colored in blue and the surrounding area is marked in green. The six electrodes and the ground/shield plane, which are excluded from the triangulation process, are colored in white. All colors are associated with the permittivity value of the material, e.g., permittivity of the surrounding area (air) $\varepsilon_r = 1$. (b) The image section shows the gap between the electrodes and the region of interest. There must be at least two finite elements due to the specific implementation to ensure a proper reconstruction. The rounding on the left- and right-hand side of the electrodes and the gaps between electrodes and grasper avoid acute angles during the meshing process. It should be noted that the distance between $\partial\Omega$ (border of Ω_{ROI}) and the border of the surrounding area must be sufficiently large. In addition, all electrodes must be surrounded by the same domain.

3.3 Calibration Method

To obtain a feasible reconstruction result, a calibration is necessary in advance to overcome certain measurement and modeling errors, e.g., discretization errors, different geometries, parasitic effects, un-modeled physical effects, etc. Therefore, an offset-gain calibration as previously used for the magnetic sensing part in Section 2.4 is used for the ECT as well. The following equation shows how the real value of $\boldsymbol{c_{true}}$ is calculated for a single capacitance measurement C [NZWF11]:

$$c_{true} = c_{\text{air}} + \underbrace{\frac{c_{\text{cube}} - c_{\text{air}}}{C_{\text{cube}} - C_{\text{air}}}}_{k} \left(C - C_{\text{air}}\right), \tag{3.14}$$

where $\boldsymbol{C}$ denotes the latest measurement data of all capacitances. $\boldsymbol{C_{cube}}$ and $\boldsymbol{C_{air}}$ represent the measured capacitance matrix of the calibration process where Ω_{ROI} is fully filled with a cube ($\varepsilon_r = 3.5$) and empty (absence of an object $\varepsilon_r = 1$), respectively. The cube, 9 cm × 5 cm × 15 cm in size, is made of polyvinyl chloride (PVC). The computed solutions of the forward problem for Ω_{ROI} set to $\varepsilon_r = 3.5$ and $\varepsilon_r = 1$ are denoted by $\boldsymbol{c_{\text{cube}}}$ and $\boldsymbol{c_{\text{air}}}$, respectively.

The gain correction factor k influences the range of the permittivity distribution to be reconstructed. The chosen k can be used for applications with a great variety between the lowest and highest occurring permittivity. For other applications a different gain correction factor is recommended. See [NZWF11] for further details about the choice of the gain correction factor.

3.4 Reconstruction Methods

Figure 3.5 shows the schematic representation of the necessary components of the ECT system to obtain a reconstruction result. Many reconstruction methods exists and are currently in use, e.g., linear back projection (LBP), optimal approximation like optimal first or second order approximation (OFOA, OSOA), non-linear reconstruction based on the Gauss-Newton scheme or Markov Chain Monte Carlo (MCMC) based methods.

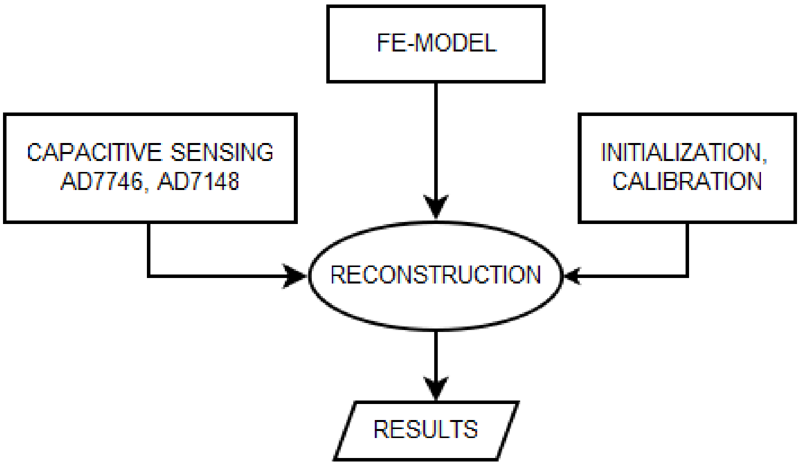

Figure 3.5: Block diagram of process steps resulting in a reconstruction result.

The LBP technique has its origin in the field of X-ray tomography, mapping the measured capacitances and permittivity distribution in ROI linear. The big advantage of this method is the high speed, although this comes with the essential drawback of image blurring. Among other things the blurring occurs due to the linear mapping approach because in reality the relation between capacitance and permittivity is non-linear (field-strength inhomogeneities, permittivity perturbation) [Bra07].

Non-linear reconstruction methods based on Gauss-Newton scheme, e.g., [BHW03] improve the accuracy of the reconstructed images which comes with additional computational afford.

Another approach could be to use statistical inversion theory leading to MCMC techniques using Metropolis Hastings (MH) or GIBBS sampler algorithm [KS05].

In this work two different kinds of reconstruction methods are taken from [Neu11] to solve the inverse problem. A deterministic approach based on Broyden-Fletcher-Goldfarb-Shanno's (BFGS) method which can be used to solve non-linear optimization problems [NF10]. The second approach to solve the inverse problem is from the statistical inversion theory called bimodal GIBBS sampler [Neu11].

3.4.1 BFGS

The BFGS-based algorithm is a deterministic algorithm which means that the reconstruction result does not change as long as the input data does not change. In other words, same input creates same output every time. To obtain the reconstruction result the inverse problem formally written as

$$\varepsilon^* = \arg\ \min_{\varepsilon} \left\{ \frac{1}{2} \left\| \boldsymbol{\Gamma} \underbrace{\left(\boldsymbol{q}(\varepsilon) - \boldsymbol{q}_{\text{meas}} \right)}_{\boldsymbol{r}} \right\|_2^2 + \frac{1}{2} \alpha \underbrace{\varepsilon^T \boldsymbol{L}^T \boldsymbol{L} \varepsilon}_{R} \right\} \tag{3.15}$$

must be solved, where, α and R denote the regularization parameter and regularization term, respectively. As mentioned earlier, this is necessary due to the ill-posed property of the problem. The regularization matrix $\boldsymbol{L}$ takes the prior knowledge into account by embedding smoothness assumptions. $\boldsymbol{q}(\varepsilon)$ and $\boldsymbol{q}_{\text{meas}}$ are the solution of the forward problem for a given permittivity distribution and the current measurement data, respectively. Thus, $\boldsymbol{r}$ is the residual describing the mismatch between model output and the measured data. The measurement noise is considered by $\boldsymbol{\Gamma}$ which can be obtained by the Cholesky triangle $\boldsymbol{\Gamma}^T\boldsymbol{\Gamma} = \boldsymbol{\Sigma}_{\boldsymbol{\nu}}^{\boldsymbol{-1}}$, where $\boldsymbol{\Sigma}_{\boldsymbol{\nu}}^{\boldsymbol{-1}}$ is the inverse covariance matrix of the measurement noise. The factor $\frac{1}{2}$ is used due to esthetically reasons. It has no influence on the result and therefore it can also be neglected. [NF10].
The minimization problem 3.15 can be solved iteratively as described in [Fle87] using

$$\varepsilon_{k+1} = \varepsilon_k - s \left(\boldsymbol{J}^T \boldsymbol{J} + \alpha \boldsymbol{L}^T \boldsymbol{L} \right)^{-1} \left(\boldsymbol{J}^T \boldsymbol{r}_k + \boldsymbol{L}^T \boldsymbol{L} \varepsilon_k \right). \tag{3.16}$$

The step size denoted by s can be set individually. The second term is also known as inverse Hessian matrix given as

$$\boldsymbol{H}_k^{-1} = \left(\boldsymbol{J}^T \boldsymbol{J} + \alpha \boldsymbol{L}^T \boldsymbol{L} \right)^{-1} \tag{3.17}$$

and the gradient of equation 3.15 is given by

$$\boldsymbol{g}_k = \boldsymbol{J}^T \boldsymbol{r}_k + \boldsymbol{L}^T \boldsymbol{L} \varepsilon_k \tag{3.18}$$

The calculation of the gradient requires $\boldsymbol{J}^T \boldsymbol{r}_k$ determined using the Green's functions to speed up the computing time [NF10].

The BFGS algorithm is a class of quasi-Newton methods with the basic iteration structure as follows

- ***a*)** Set $\boldsymbol{p}_k = -\boldsymbol{H}_k^{-1} \boldsymbol{g}_k$
- ***b*)** Search s giving $\varepsilon_{k+1} = \varepsilon_k + s\boldsymbol{p}_k$ and update $\boldsymbol{s}_k = s\boldsymbol{p}_k$
- ***c*)** Update $\boldsymbol{z}_k = \boldsymbol{g}\left(\varepsilon_{k+1}\right) - \boldsymbol{g}\left(\varepsilon_k\right)$
- ***d*)** Determine $\boldsymbol{H}_{k+1}^{-1} = \boldsymbol{H}_k^{-1} + \left(\frac{\boldsymbol{s}_k^T \boldsymbol{z}_k + \boldsymbol{z}_k^T \boldsymbol{H}_k^{-1} \boldsymbol{z}_k}{\left(\boldsymbol{s}_k^T \boldsymbol{z}_k\right)^2}\right) \boldsymbol{s}_k \boldsymbol{s}_k^T - \frac{\boldsymbol{H}_k^{-1} \boldsymbol{z}_k \boldsymbol{s}_k^T + \boldsymbol{s}_k \boldsymbol{z}_k^T \boldsymbol{H}_k^{-1}}{\boldsymbol{s}_k^T \boldsymbol{z}_k}$

The parameters s, α, ε_{min}, ε_{max} and number of iterations must be set in advance [NF10]. The obtained reconstruction results of the BFGS algorithm for rod-like inclusions are shown in Section 3.5.

3.4.2 Bimodal GIBBS Sampler

In statistical inversion theory the bimodal GIBBS sampler is a special case of the MCMC method. Instead of generating a single estimate as done using, e.g., BFGS, the statistical approach produces a distribution to get estimates providing additional information about the solution [KS05].
Statistical inversion theory is based on the Bayes' rule

$$p(A|B) = \frac{p(B|A)p(A)}{p(B)} \propto p(B|A)p(A) \tag{3.19}$$

or rewritten to stay conform with the used nomenclature

$$p(\varepsilon|\boldsymbol{q}_{\text{meas}}) = \frac{p(\boldsymbol{q}_{\text{meas}}|\varepsilon)p(\varepsilon)}{p(\boldsymbol{q}_{\text{meas}})} \propto p(\boldsymbol{q}_{\text{meas}}|\varepsilon)p(\varepsilon) \tag{3.20}$$

where $p(\varepsilon|\boldsymbol{q}_{\text{meas}})$ and $p(\varepsilon)$ denote the posterior and prior distribution, respectively. The evidence and likelihood functions are expressed by $p(\boldsymbol{q}_{\text{meas}})$ and $p(\boldsymbol{q}_{\text{meas}}|\varepsilon)$, respectively. However, the evidence $p(\boldsymbol{q}_{\text{meas}})$ can be dropped because it acts like a normalization factor. The prior distribution $p(\varepsilon)$ is used to model the prior knowledge about the permittivity distribution. The prior distribution is essential in inversion theory because it must reflect the prior information in a feasible way. In this case it can be written as

$$p(\varepsilon) \propto \exp\left(-\frac{1}{2}\alpha\varepsilon^T \boldsymbol{L}^T \boldsymbol{L}\varepsilon\right). \tag{3.21}$$

The likelihood function expresses the interrelationship between the measured data and the permittivity distribution. For additive Gaussian noise it can be written as

$$p(\boldsymbol{q}_{\text{meas}}|\varepsilon) \propto \exp\left(-\frac{1}{2}\left(\boldsymbol{q}(\varepsilon) - \boldsymbol{q}_{\text{meas}}\right)^T \Sigma_\nu^{-1} \left(\boldsymbol{q}(\varepsilon) - \boldsymbol{q}_{\text{meas}}\right)\right). \tag{3.22}$$

Here, Σ_ν denotes the covariance matrix of the measurement noise.

Finally, the posteriori distribution can be written as

$$p\left(\varepsilon|\boldsymbol{q}_{\text{meas}}\right) \propto \exp\left(-\frac{1}{2}\left(\boldsymbol{q}(\varepsilon) - \boldsymbol{q}_{\text{meas}}\right)^T \Sigma_\nu^{-1} \left(\boldsymbol{q}(\varepsilon) - \boldsymbol{q}_{\text{meas}}\right)\right) \exp\left(-\frac{1}{2}\alpha\varepsilon^T \boldsymbol{L}^T \boldsymbol{L}\varepsilon\right) I(\varepsilon), \tag{3.23}$$

where $I(\varepsilon)$ is an indicator function to enforce that the algorithm is bimodal [Neu11]. There are several ways to evaluate the posterior distribution. Commonly, a maximum a posteriori (MAP), a conditional mean (CM) or an ML estimate is used. Another approach is to use, e.g., MCMC techniques, which is an effective class of random sampling methods. The idea of MCMC is to draw samples which support the posterior distribution. In other words, a sample is a supporting point of the distribution. These samples are generated using a Markov Chain. Later on the generated samples are used for the Monte Carlo integration (approximate integration). The transition kernel of the Markov Chain is realized using a bimodal GIBBS sampler which comes with the advantage that a proposal is always accepted in comparison to, e.g., the MH algorithm [KS05]. Therefore, the bimodal GIBBS sampler from [Neu11] was used. It should be noted that bimodal indicates that the algorithm can only be used for distributions with two different permittivity values. Detailed information about the algorithm and the implementation can be found in [Neu11].

3.5 Results

This section presents the obtained results for the ECT using the deterministic reconstruction algorithm BFGS (see 3.5.1) and the statistical approach using a bimodal GIBBS sampler (see 3.5.2). The parameters of the BFGS algorithm were set as follows. The regularization parameter $\alpha = 10^{-9}$, the step size $s = 0.01$ and the maximum number of iterations to 200. The regularization parameter of the GIBBS sampler was set to $\alpha = 10^{-6}$.

3.5.1 BFGS

Figures 3.6 and 3.7 show the reconstruction results for different objects in the vicinity of the electrodes. In both cases the reconstructed position of the object matches the true position of the object. As already mentioned in the magnetic sensing part due to the soft field properties of the ECT, neither the shape nor the radius of the reconstructed object can be determined accurately.

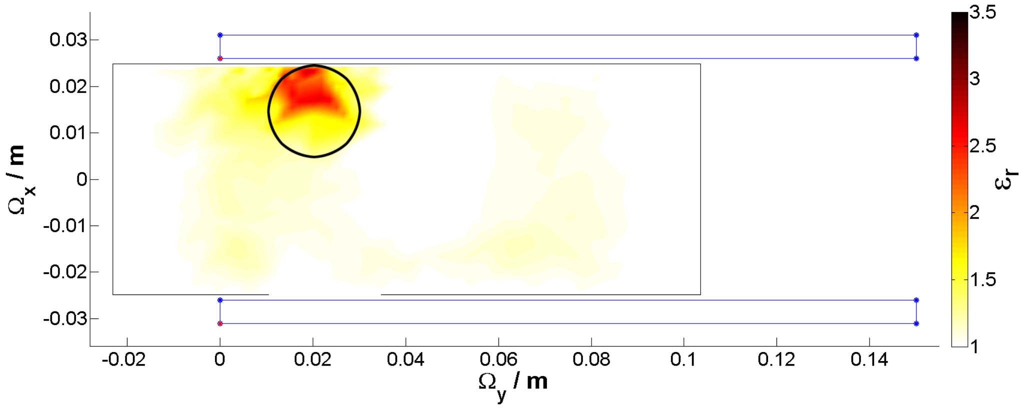

Figure 3.6: Snapshot of the reconstruction result of the BFGS algorithm where a rod made of PVC, 10.5 mm in radius, is positioned in Ω_{ROI}. The black circle depicts the true position of the semicircular rod at x = 25 mm and y = 20 mm and the color bar illustrates the value of the relative permittivity. The blue and black rectangles represent the parallel jaw gripper (grasper) and Ω_{ROI}, respectively. The area with the highest relative permittivity (red and orange) shows the position of the inclusion. This area matches the true position of the rod.

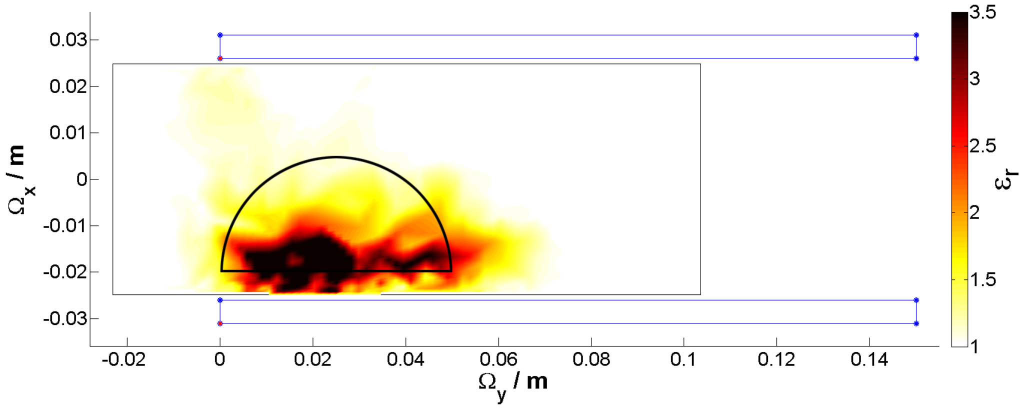

Figure 3.7: Snapshot of the reconstruction result of the BFGS algorithm where a semicircular rod made of PVC, 25 mm in radius, is positioned in Ω_{ROI}. The black semicircle depicts the true position of the PVC rod at x = 5 mm and y = 25 mm and the color bar illustrates the value of the relative permittivity. The blue and black rectangles represent the parallel jaw gripper (grasper) and Ω_{ROI}, respectively. The area with the highest relative permittivity (black, red, orange and yellow) shows the position of the inclusion. This area matches the true position of the semicircular rod.

The sensing range (sensitivity) of the ECT using the BFGS algorithm is shown in Figure 3.8 in detail. The two snapshots show two reconstructions which become borderline due to the position of the PVC rod. This is due to the decreasing sensitivity of the ECT system on the left- and right-hand side of the grasper (viewed from the top) because no electrodes can be mounted on those sides. The artifacts in the center of Ω_{ROI} are caused by the increasing distance between the rod and the electrodes. Therefore, the best reconstruction results can be obtained in the vicinity of the electrodes.

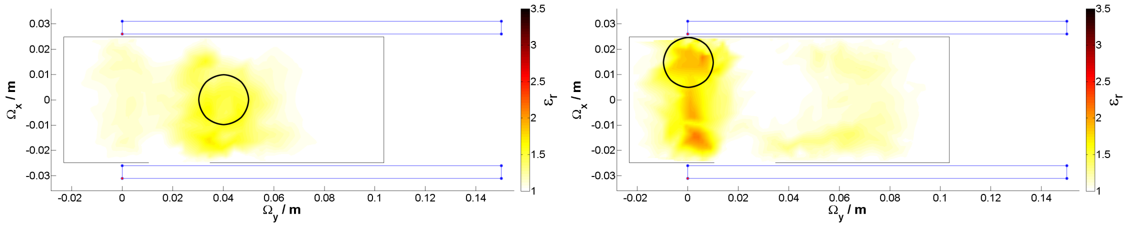

(a)

(b)

Figure 3.8: Sensitivity of the reconstruction process using the BFGS algorithm. The color bar illustrates the value of the relative permittivity. The blue and black rectangles represent the parallel jaw gripper (grasper) and Ω_{ROI}, respectively. (a) Snapshot of the reconstruction result where a rod made of PVC, 10.5 mm in radius, is positioned in Ω_{ROI}. The black circle depicts the true position of the PVC rod at x = 10 mm and y = 40 mm. The area with the highest relative permittivity (yellow) shows where the object could be positioned. This area is much larger than the size of the rod. However, the true position of the inclusion is still inside this area. (b) Snapshot of the reconstruction result with the same rod as used in (a), is positioned at x = 25 mm and y = 0 mm depicted by the black circle. The area with the highest relative permittivity (orange) shows where the object could be positioned. This area is much larger than the size of the rod. However, the true position of the inclusion is still inside this area.

Figure 3.9 shows that the reconstructed permittivity distribution for an empty gripper (air $\varepsilon_r = 1$) matches very well after the offset-gain calibration was done.

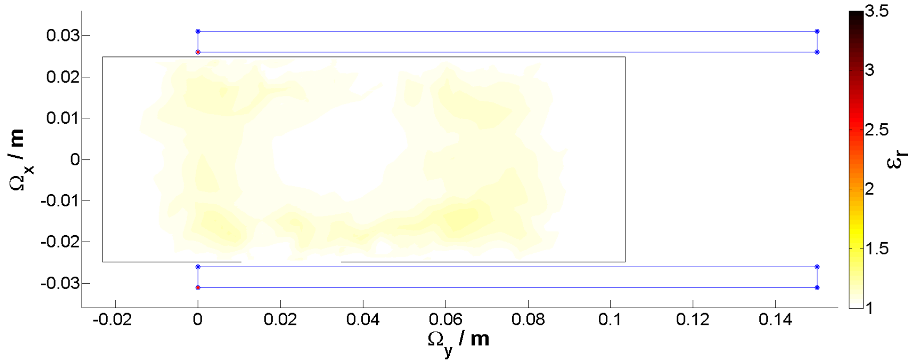

Figure 3.9: Snapshot of the reconstructed permittivity distribution in Ω_{ROI} with no inclusion. The color bar depicts the relative permittivity. The blue and black rectangles represent the parallel jaw gripper (grasper) and Ω_{ROI}, respectively.

3.5.2 Bimodal GIBBS Sampler

Figure 3.10 shows the sensing range of the ECT using the bimodal GIBBS sampler in detail. A snapshot of the online reconstruction (mean estimate of all samples of the MCMC output) with no inclusion in Ω_{ROI} and the corresponding uncertainty is presented. In Figure 3.10(a) the artifacts on the left- and right-hand side as well as in the center of Ω_{ROI} are caused by the same reasons (no electrodes mounted on those sides and increasing distance to the electrodes) as already discussed for the BFGS algorithm. These artifacts must be considered for the localization of inclusions as well. The big advantage of the bimodal GIBBS sampler in comparison to the deterministic BFGS algorithm is that it not only provides a single result but it also gives information about the uncertainty of the reconstructed result. The associated uncertainty shown in Figure 3.10(b) increases towards the left- and right-hand side and also in the center.

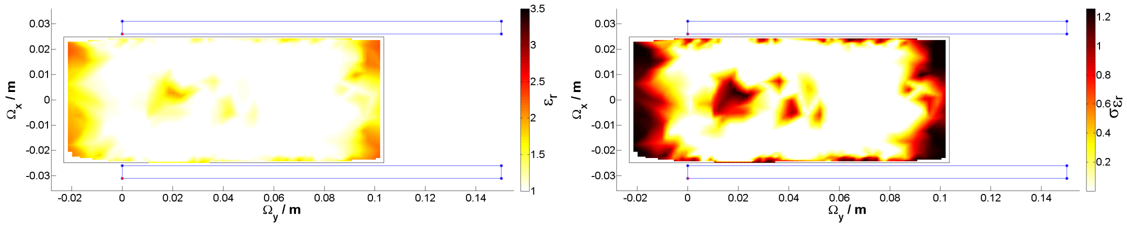

(a) (b)

Figure 3.10: Sensing range of the ECT using the bimodal GIBBS sampler. The color bar depicts the relative permittivity. The blue and black rectangles represent the grasper and Ω_{ROI}. (a) Snapshot of the reconstruction result with no inclusion. The artifacts are caused by the decreasing sensitivity in these areas. (b) Standard deviation of the reconstruction result. The uncertainty increases in the areas where the sensitivity decreases.

Figures 3.11, 3.12 and 3.13 show the reconstruction results for PVC objects different in shape and size placed at different positions in Ω_{ROI}. In all cases the position can be reconstructed feasibly with remaining artifacts. It should be noted that most of these artifacts are already visible in the reconstruction where Ω_{ROI} is empty. The artifacts of the empty reconstruction occur in all the presented results and must be considered, otherwise a localization of an inclusion is not possible.

The uncertainty in all presented results is at a high level which increases the computational time to obtain the result. To obtain a usable reconstruction result the log-posterior function must reach and stay in the equilibrium. This is true for all presented reconstruction results.

Comparing the results of Figures 3.11 and 3.12, the reconstruction of the object in the center of Ω_{ROI} is located more feasibly than the object in the vicinity of the electrodes. This behavior of the GIBBS sampler stands in contrast to the obtained behavior of the

BFGS algorithm. As already mentioned above, due to the soft field properties of the ECT neither the shape nor the radius of the reconstructed object can be determined accurately.

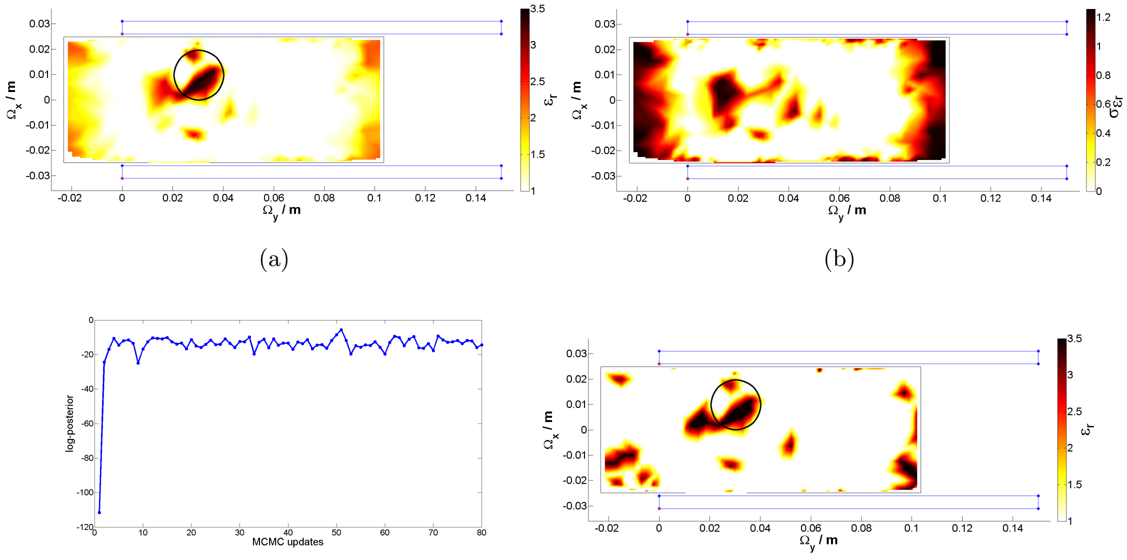

(a) (b)

(c) (d)

Figure 3.11: (a) Snapshot of the reconstruction result (mean estimate of all samples of the MCMC output) where a rod made of PVC, 10.5 mm in radius, is positioned in Ω_{ROI}. The black circle depicts the true position of the PVC rod at $\mathrm{x} = 20\,\mathrm{mm}$ and $\mathrm{y} = 30\,\mathrm{mm}$ and the color bar illustrates the value of the relative permittivity. The blue and black rectangles represent the grasper and Ω_{ROI}, respectively. The area with the highest relative permittivity (black and red) shows the position of the inclusion. This area matches the true position of the rod. (b) Standard deviation of the reconstruction result. It reflects the low sensitivity in the center, on the left- and right-hand side of Ω_{ROI}. (c) MCMC output trace of the log-posterior function. It reaches the equilibrium after twelve updates. (d) Sample of the MCMC output where the log-posterior function is at its maximum.

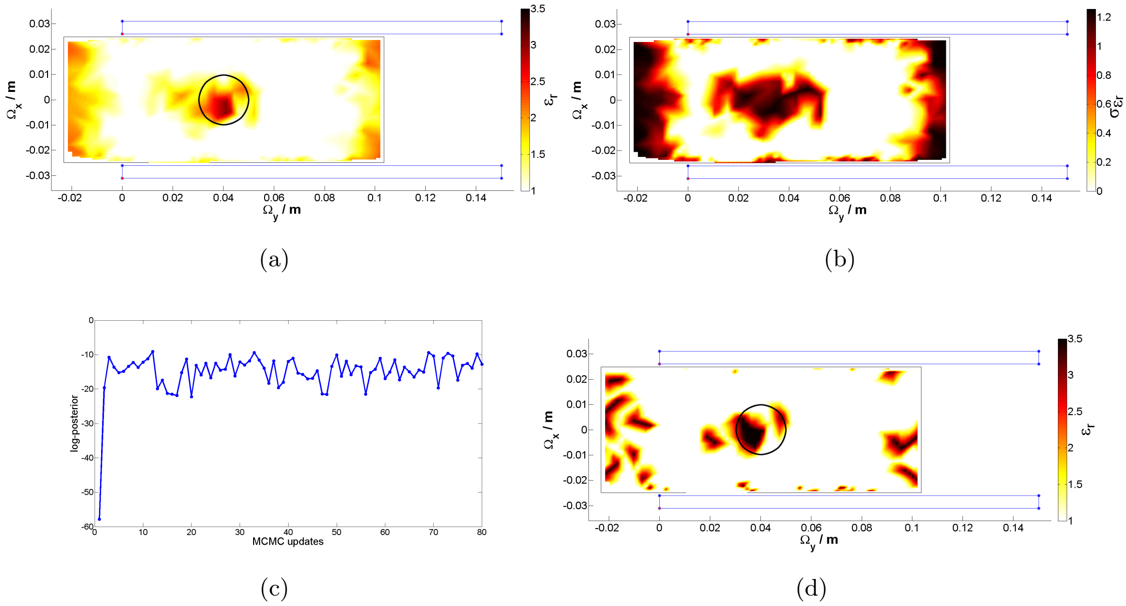

(a) (b)

(c) (d)

Figure 3.12: (a) Snapshot of the reconstruction result (mean estimate of all samples of the MCMC output) where a rod made of PVC, 10.5 mm in radius, is positioned in Ω_{ROI}. The black circle depicts the true position of the PVC rod at $x = 10$ mm and $y = 40$ mm and the color bar illustrates the value of the relative permittivity. The blue and black rectangles represent the grasper and Ω_{ROI}, respectively. The area with the highest relative permittivity (black and red) shows the position of the inclusion. This area matches the true position of the rod. (b) Standard deviation of the reconstruction result. It reflects the low sensitivity in the center, on the left- and right-hand side of Ω_{ROI}. (c) MCMC output trace of the log-posterior function. It reaches the equilibrium after fifteen updates. (d) Sample 60 of the MCMC output trace.

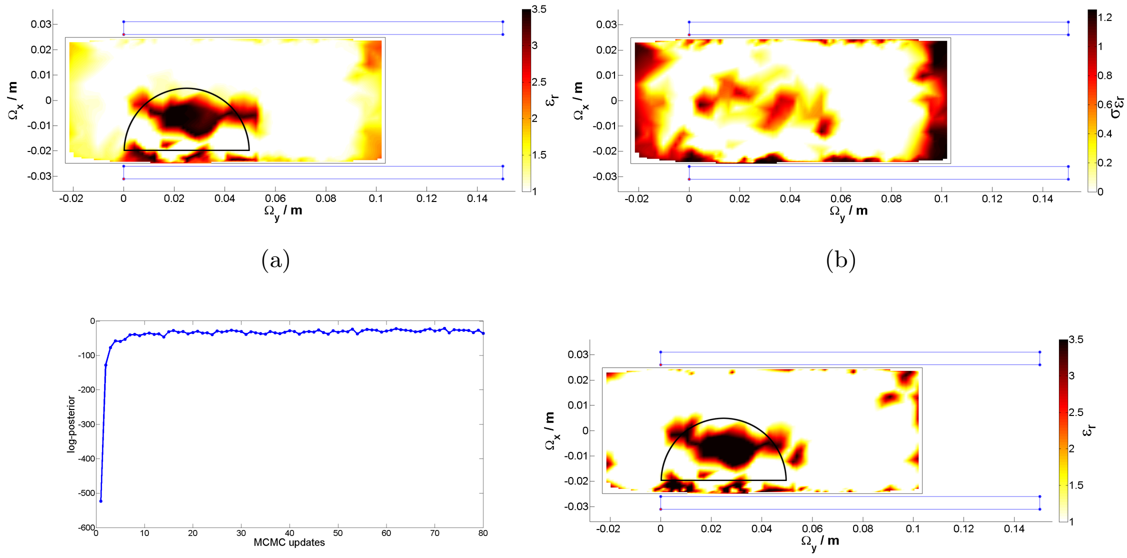

(a) (b) (c) (d)

Figure 3.13: (a) Snapshot of the reconstruction result (mean estimate of all samples of the MCMC output) where a semicircular rod made of PVC, 25 mm in radius, is positioned in Ω_{ROI}. The black semicircle depicts the true position of the inclusion at x = 5 mm and y = 25 mm and the color bar illustrates the value of the relative permittivity. The blue and black rectangles represent the grasper and Ω_{ROI}, respectively. The area with the highest relative permittivity (black and red) shows the position of the inclusion. This area matches the true position of the semicircular rod. (b) Standard deviation of the reconstruction result. It reflects the low sensitivity in the center, on the left- and right-hand side of Ω_{ROI}. (c) MCMC output trace of the log-posterior function. It reaches the equilibrium after ten updates. (d) Sample of the MCMC output where the log-posterior function is at its maximum.

Chapter 4

Prototype

This chapter gives an overview of the developed prototype for the pretouch sensing system. At the beginning the grasper is presented in Section 4.1. Sections 4.2 and 4.3 describe the mobile unit and the stationary unit. The two possible measurement setups can be found in Section 4.4.

To realize the pretouch sensing system as described in Chapter 1 a prototype was developed which consists of two parts. First, the mobile unit includes the data acquisition and the transmitter module (TM). Second, the stationary unit includes the receiver and the data processing module. The receiver module is an optional part increasing the flexibility of the prototype. Figures 4.1, 4.2 and 4.3 depict the prototype and two measurement setups.

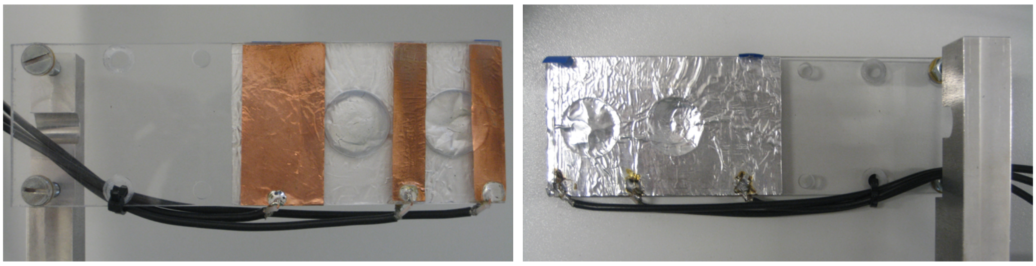

(a)

(b)

Figure 4.1: (a) Electrodes on front side of the grasper. (b) Ground/shield plane on the backside of the parallel jaw gripper.

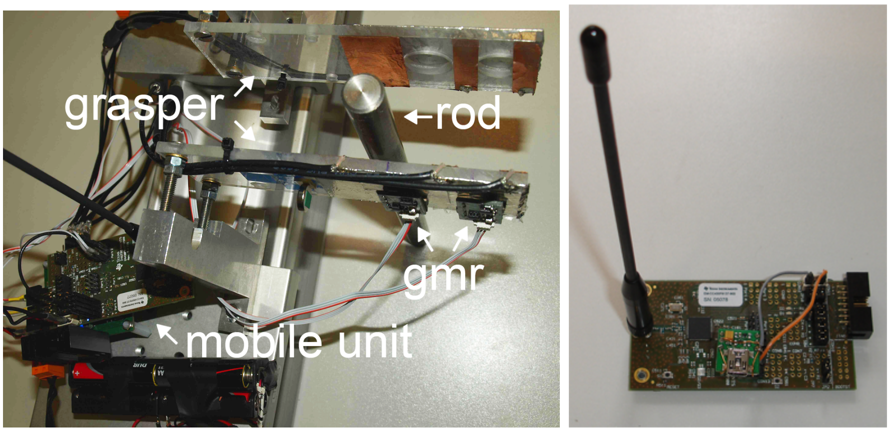

(a) (b)

Figure 4.2: (a) Prototype of the mobile unit and grasper. (b) Receiver module of the stationary unit.

4.1 Grasper

The grasper is a parallel jaw gripper, 15 cm × 5 cm × 0.5 cm in size, mounted on a translation stage. Two GMR sensors are aligned with the permanent magnet on the backside of the grasper measuring the magnetic field in the interior of the grasper as described in Chapter 2. The distance between the first and second GMR sensor and the permanent magnet is 70 mm and 40 mm, respectively.

For the ECT system six electrodes (three on each side) are mounted symmetrically on the left and right side of the parallel jaw gripper. The electrodes, four 1 cm × 5 cm and two 2.5 cm × 5 cm in size are glued onto the surface of the grasper as shown in Figure 4.1(a). The ground/shield plane is glued onto the backside of the grasper as shown in Figure 4.1(b).

4.2 Mobile Unit

The mobile unit is battery powered (12 V) and can easily be mounted on a grasper's gripper arm. It consists of a TM and a data acquisition module (capacitive measurement printed circuit board (PCB)) stacked onto each other. The TM is an *EM430F6317RF900 Evaluation Module* from Texas Instruments. The mobile unit provides up to six power supply outputs and eight data inputs for GMR sensors mounted on the GMR PCB. Two of them are in use for this prototype.

For the ECT, the mobile unit provides up to six inputs (all of them are in use) for electrodes. All inputs are connected to a switch matrix to reroute the electrodes either

to the input of AD7746 or AD7148. Due to the limited number of inputs of the switch matrix channel one (CIN1) of AD7746 and seven channels (CIN0 - CIN6) of AD7148 are connected to the switch matrix. The remainder of both capacitive sensing chips cannot be used with this hardware.
See Appendix B for further hardware-related details, e.g., schematics and layouts.

4.3 Stationary Unit

The stationary unit consists of the receiver module and a host computer. The receiver module forwards the received sensor data to the host computer running a client application (CA) where all reconstruction processes for the magnetic sensing and ECT as shown in Figures 2.1 and 3.5 take place. The stationary unit is powered via the USB of the host computer. For the receiver module the same *EM430F6317RF900 Evaluation Module* from Texas Instrument as for the TM was used.

4.4 Measurement Setup

In measurement setup A, shown in Figure 4.3(a), the TM of the mobile unit communicates via a radio frequency (RF) link with the receiver module of the stationary unit and forwards the raw sensor data. In measurement setup B, shown in Figure 4.3(b), the receiver module of the stationary unit is not used and the raw sensor data is forwarded to the host computer directly. Comparing the two measurement setups, A is more flexible due to increased mobility which comes with the RF link between the mobile and stationary unit.
Further software-related details on how to run both measurement setups can be found in Appendix A.

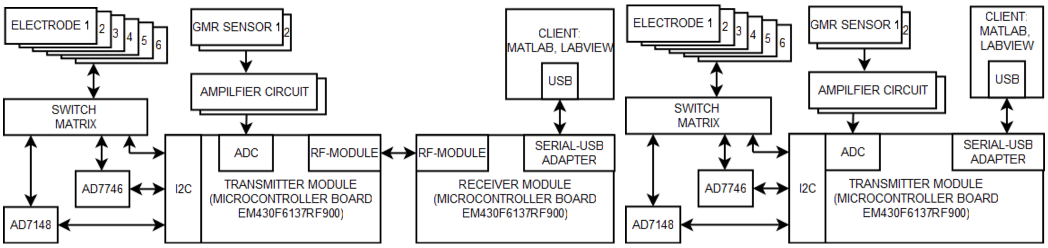

(a) (b)

Figure 4.3: Block diagram of two possible measurement setups. (a) Measurement setup A including the RF link and (b) B without RF link.

Chapter 5

Reconstruction Results of the Pretouch Sensor System

This chapter presents the reconstruction results of the pretouch sensing system running the magnetic sensing system (MSS) and the electrical capacitance tomography (ECT) simultaneously. In Section 5.1, the results of the MSS and the $\mathrm{ECT}_{\mathrm{BFGS}}$ algorithm are presented. The MSS and $\mathrm{ECT}_{\mathrm{GIBBS}}$ algorithm results are shown in Section 5.2.

For all measurements two objects are placed in the Ω_{ROI} to examine if the system is able to distinguish the objects based on the material properties. The first object is either a rod, 10.5 mm in radius, or a semicircular rod, 25 mm in radius. The second object is a rod made of steel, 3 mm in radius. The position of the objects is depicted in the figures. It should be noted that the length of the Ω_{ROIy} for the MSS and $\mathrm{ECT}_{\mathrm{BFGS}}/\mathrm{ECT}_{\mathrm{GIBBS}}$ is offset shifted by 40 mm. Thus, $\Omega_{\mathrm{MSS\ ROI\ y}} = 40\ mm$ equals $\Omega_{\mathrm{ECT\ ROI\ y}} = 0\ mm$.
The parameters values from Section 3.5 were used for the $\mathrm{ECT}_{\mathrm{BFGS}}$ and $\mathrm{ECT}_{\mathrm{GIBBS}}$ algorithm.

5.1 MSS and $\mathrm{ECT}_{\mathrm{BFGS}}$ Reconstruction

Figures 5.1, 5.2 and 5.3 show the results of the $\mathrm{ECT}_{\mathrm{BFGS}}$ and MSS in comparison. As expected, the PVC rod does not influence the MSS. The true position of the steel rod matches the result of the MSS in all cases. In case of the ECT system the steel rod should be visible in the reconstruction results of the $\mathrm{ECT}_{\mathrm{BFGS}}$. However, this is not the case in all three presented results. This can be explained because the calibration of the system was done using a PVC cube with a permittivity of $\varepsilon_r = 3.5$. Therefore, the calculated correction factor k is not appropriate for inclusions with a very high permittivity. Another factor is that high permittivity values are clipped. Therefore, the steel rod is not visible in the reconstruction results. The reconstructions of the positions of the PVC inclusions are still feasible. Therefore, the pretouch sensing system using the ECT$_{\mathrm{BFGS}}$ algorithm is usable for object recognition and localization based on their material properties, i.e. relative permittivity and relative permeability.

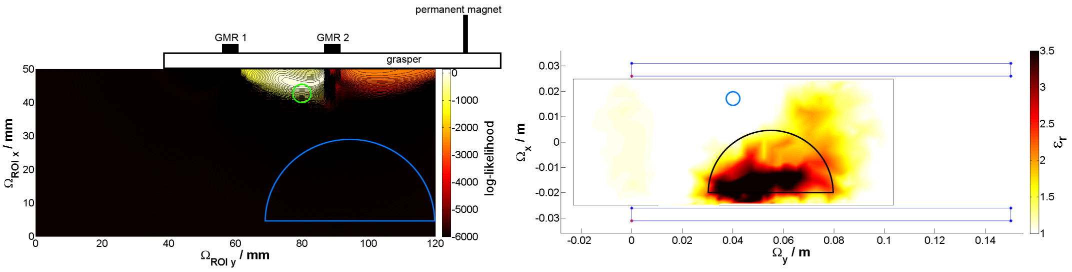

(a) (b)

Figure 5.1: Snapshots of the online reconstruction. (a) The green circle and the blue semicircle depict the true position of the steel rod and the PVC semicircular rod, respectively. The maximum of the log-likelihood (color bar) is the MLE. The color shades show how likely it is for an object to be positioned at a certain place. The MLE and the true position of the steel rod (top center of the green circle) have a close match. (b) The black semicircle and the blue circle depict the true position of the PVC semicircular rod and the steel rod, respectively. The blue and black rectangles represent the grasper and Ω_{ROI}. The area with the highest relative permittivity (black, red and orange) shows the position of the inclusion. This area matches the true position of the semicircular rod. The artifacts at the top right are due to the decreasing sensitivity in this area.

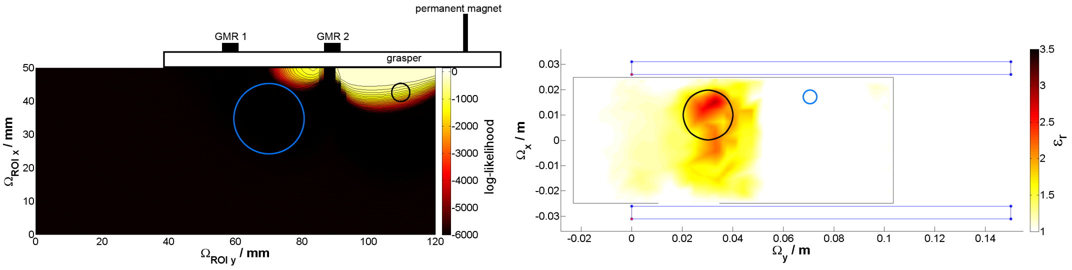

(a) (b)

Figure 5.2: Snapshots of the online reconstruction. (a) The black and blue circles depict the true position of the steel rod and the PVC rod, respectively. The maximum of the log-likelihood (color bar) is the MLE. The color shades show how likely it is for an object to be positioned at a certain place. The MLE and the true position of the steel rod (top center of the black circle) have a close match. (b) The black and blue circles depict the true position of the PVC rod and the steel rod, respectively. The blue and black rectangles represent the grasper and Ω_{ROI}. The area with the highest relative permittivity (red and orange) shows the position of the inclusion. This area matches the true position of the rod.

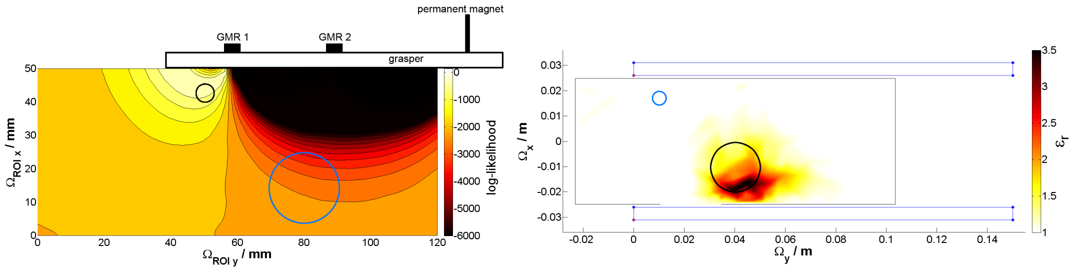

(a) (b)

Figure 5.3: Snapshots of the online reconstruction. (a) The black and blue circles depict the true position of the steel rod and the PVC rod, respectively. The maximum of the log-likelihood (color bar) is the MLE. The color shades show how likely it is for an object to be positioned at a certain place. The MLE and the true position of the steel rod (top center of the black circle) have a close match. (b) The black and blue circles depict the true position of the PVC rod and the steel rod, respectively. The blue and black rectangles represent the grasper and Ω_{ROI}. The area with the highest relative permittivity (black, red and orange) shows the position of the inclusion. This area matches the true position of the rod.

5.2 MSS and ECT$_{\mathrm{GIBBS}}$ Reconstruction

Figures 5.5, 5.6 and 5.4 show the results of the MSS and ECT$_{\mathrm{GIBBS}}$ in comparison. As already mentioned in the previous section the PVC rod does not influence the MSS. The true position of the steel rod matches the result of the MSS in two of three cases. In case of the ECT, the steel rod should be visible in the reconstruction results of the ECT$_{\mathrm{GIBBS}}$. However, this is not the case in all three presented results. This can be explained because the calibration of the system was done using a PVC cube with a permittivity of $\varepsilon_r = 3.5$. Therefore, the calculated correction factor k is not appropriate for inclusions with a very high permittivity. Another factor is that the Jacobian matrix is only accurate for small permittivity values. In addition, high permittivity values are clipped. Therefore, the steel rod is not visible in the reconstruction results. The reconstructions of the positions of the PVC inclusions are borderline but still usable with a slightly increased number of artifacts in comparison to the results of Section 3.5.2. Again, the artifacts of the reconstruction where Ω_{ROI} was empty must be considered for the localization of inclusions. In comparison to the results of the ECT$_{\mathrm{GIBBS}}$ and MSS, the results of the deterministic ECT$_{\mathrm{BFGS}}$ and MSS approach are slightly better . However, the pretouch sensing system using the ECT$_{\mathrm{GIBBS}}$ and MSS is still usable for object recognition and localization based on the object's material properties, i.e. relative permittivity and relative permeability.

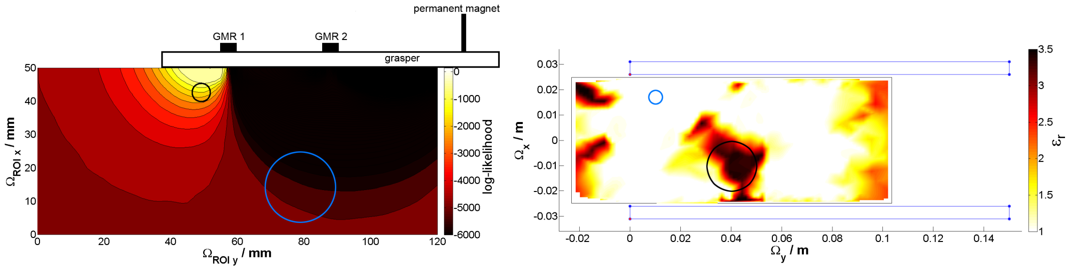

(a) (b)

Figure 5.4: Snapshots of the online reconstruction. (a) The black and blue circles depict the true position of the steel rod and the PVC rod, respectively. The maximum of the log-likelihood (color bar) is the MLE. The color shades show how likely it is for an object to be positioned at a certain place. The MLE and the true position of the steel rod (top center of the black circle) have a close match. (b) The black and blue circles depict the true position of the PVC rod and the steel rod, respectively. The blue and black rectangles represent the grasper and Ω_{ROI}. The area with the highest relative permittivity (black and red) shows the position of the inclusion. This area matches the true position of the rod.

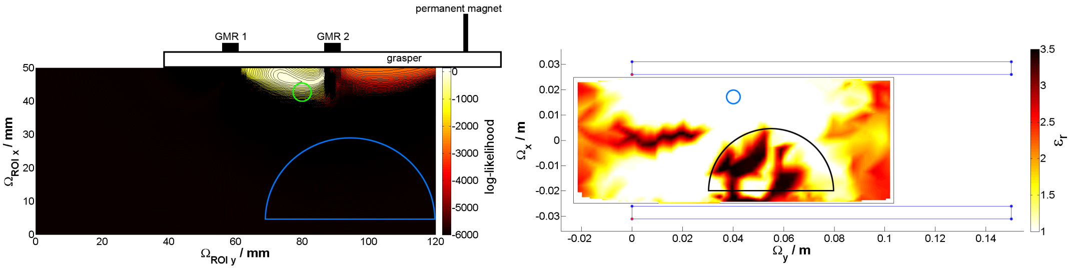

(a) (b)

Figure 5.5: Snapshots of the online reconstruction. (a) The green circle and the blue semicircle depict the true position of the steel rod and the PVC semicircular rod, respectively. The maximum of the log-likelihood (color bar) is the MLE. The color shades show how likely it is for an object to be positioned at a certain place. The MLE and the true position of the steel rod (top center of the green circle) have a close match. (b) The black semicircle and the blue circle depict the true position of the PVC semicircular rod and the steel rod, respectively. The blue and black rectangles represent the grasper and Ω_{ROI}. This reconstruction is borderline due to the artifacts on the left-hand side. The area with the highest relative permittivity (black and red) shows the position of the inclusion. This area includes the true position of the semicircular rod.

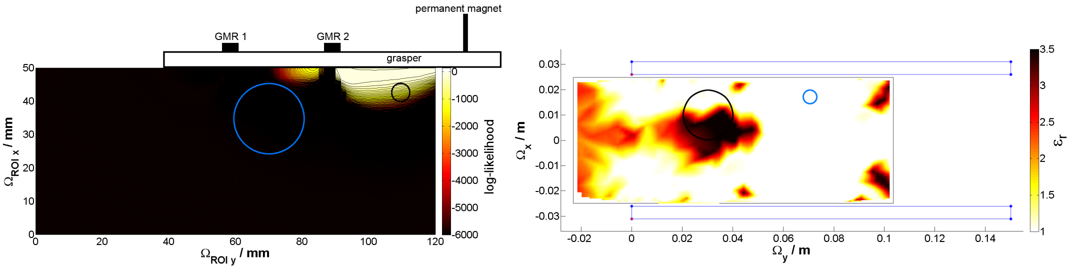

(a) (b)

Figure 5.6: Snapshots of the online reconstruction. (a) The black and blue circles depict the true position of the steel rod and the PVC rod, respectively. The maximum of the log-likelihood (color bar) is the MLE. The color shades show how likely it is for an object to be positioned at a certain place. The MLE and the true position of the steel rod (top center of the black circle) almost match. (b) The black and blue circles depict the true position of the PVC rod and the steel rod, respectively. The blue and black rectangles represent the grasper and Ω_{ROI}. This reconstruction is borderline due to the artifacts on the left-hand side. The area with the highest relative permittivity (black and red) shows the position of the inclusion. This area includes the true position of the rod.

Chapter 6

Conclusion

In this work a pretouch sensing system prototype for a grasper (parallel jaw gripper) was developed to recognize and localize objects based on their relative permeability and relative permittivity. The developed pretouch sensing system consists of two parts:
The first part is a magnetic sensing system based on GMR sensors with a sensing range covering 20 mm × 80 mm of the interior of the grasper. The developed online reconstruction algorithm includes a GP and a MLE for the position estimation. The presented results show that the magnetic approach is feasible for the localization of ferromagnetic objects.
The second part is an ECT approach to be able to localize objects based on their relative permittivity. For the capacitive sensing the applicability of two different algorithm developed at the *Institute of Electrical Measurement and Measurement Signal Processing*, *Graz University of Technology* for a pipe were examined. Based on the shown results the BFGS and the bimodal GIBBS sampler algorithm are feasible within a limited area (50 mm × 60 mm) of the interior of the grasper. This is due to the geometry and the limited number of electrodes. Furthermore, the capacitive sensing part is not yet usable for a real-time reconstruction due to the high computational effort. Further improvements of the reconstruction algorithm regarding speed are suggested in Section 6.1.
The advantages of the pretouch sensor system are that both sensors are thin (electrodes are 70 μm thick), do not need lots of space and do not influence each other. In addition, the GMR sensors and the electrodes can also be mounted beyond the surface of the grasper if necessary. Another significant benefit is the flexibility of the pretouch sensor system which comes with the wireless connection between the mobile and the stationary unit. The entire system is battery-powered and does not require lots of space. Therefore, it can easily be mounted on a different robot gripper arm. The presented results of the pretouch sensor system show that the approach can be used for an online localization and recognition of objects with respect to the material properties, i.e. relative permittivity and relative permeability.

6.1 Possible Future Work

The magnetic sensing system can be further improved and augmented by implementing the following suggestions:

- Sensing range: As already mentioned in Section 2.6 the sensing range can be augmented by increasing the number of GMR sensors and using switchable electro magnets instead of a single permanent magnet. To implement this attractive extension the field problem of Section 2.1 has to be redefined and the simulation framework has to be extended. In addition, this extension would also increase the accuracy of the reconstructed object position.
- Object shape: To increase the number of detectable object shapes. Various types of inclusions have to be used for the training.

Further improvements for the ECT algorithm:

- BFGS: The used implementation is not yet usable for a real-time reconstruction. One reason for this is the fixed step size, because the number of iterations to obtain the result depends on the step size. This limitation can be overcome by implementing a line search algorithm reducing the required number of iteration steps and improving the reconstruction speed.
- Other reconstruction techniques, such as OFOA or OSOA, are available which come with the advantage of an increased reconstruction speed.

Appendices

Appendix A

Software-related Implementation Details

This chapter describes the software for the developed prototype/measurement setup as shown in Figure 4.3. Section A.1 describes the graphical user interface (GUI) called configuration tool which was implemented with LabView. Sections A.2.1 and A.2.2 look at the software running on the mobile unit and the stationary unit. The setup of the prototype is presented in Section A.3 and the MATLAB scripts to run the reconstructions on the host computer can be found in A.4. Finally, Section A.5 provides detailed information about the configuration and measurement data messages exchanged between the TM of the mobile unit and the CA, e.g., the configuration tool or MATLAB scripts running the reconstruction, on the host computer.

A.1 Configuration Tool

The configuration tool (CT) gives full control over the mobile unit to the user. It enables the user to make any modifications of the IC's configuration of the capacitive measurement PCB, e.g., AD7746, AD7148 and ADG2128. Furthermore, the user can run different measurement sequences and can store the received measurement data in a log file if needed.

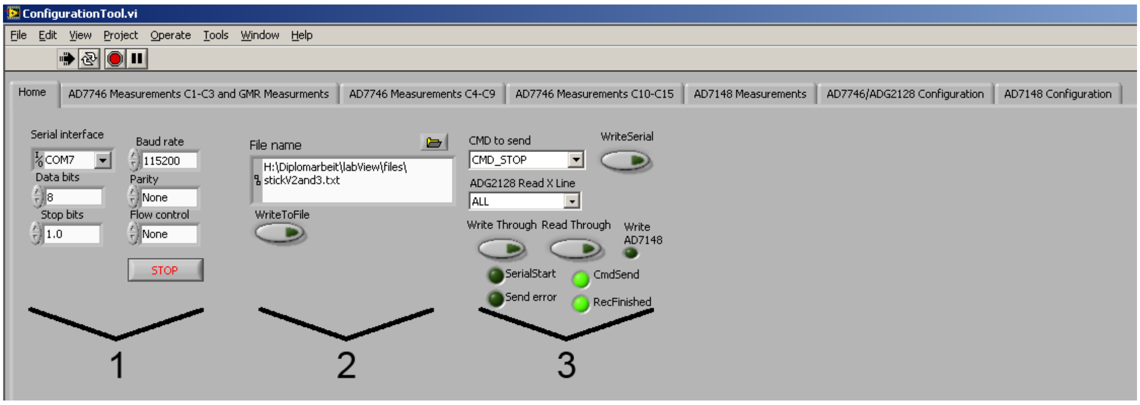

Serial interface: COM7
Baud rate: 115200
Data bits: 8
Parity: None
Stop bits: 1.0
Flow control: None
File name: H:\Diplomarbeit\labView\files\stickV2and3.txt
CMD to send: CMD_STOP
ADG2128 Read X Line: ALL

Figure A.1: Image section of the CT. It depicts the page 'Home' which is one of the seven selectable pages. In area one of the page 'Home' the serial interface can be configured, e.g., port, baud rate, data bits, parity, stop bits and flow control, where the USB to UART converter is connected. Area two is used for the data logging. Selecting the button 'WriteToFile' enables data logging at the specified place 'File name'. In area three, a new command can be sent by using the drop down menu 'CMD to send' and pressing the button 'WriteSerial'. All selectable commands are described in Table A.1. The buttons 'Write Through' and 'Read Through' enable to write and read from the shadow register or the chip register. The LEDs indicate the current status. LED 'CmdSend' indicates that the last command was sent. LED 'Serial Start' flashes once after the command is acknowledged by the stationary unit. LED 'Send error' is on when the command was not acknowledged by the mobile unit. LED 'RecFinished' flashes once when a reply of a configuration message is received completely. (It is off while receiving a reply of a configuration message consisting of more than one package.) LED 'writeAD7148' is on while transmission of a message with more than one package is not finished yet. The drop down menu 'ADG2128 Read X Line' can be used to read one specific/all line(s) of the ADG2128 register.

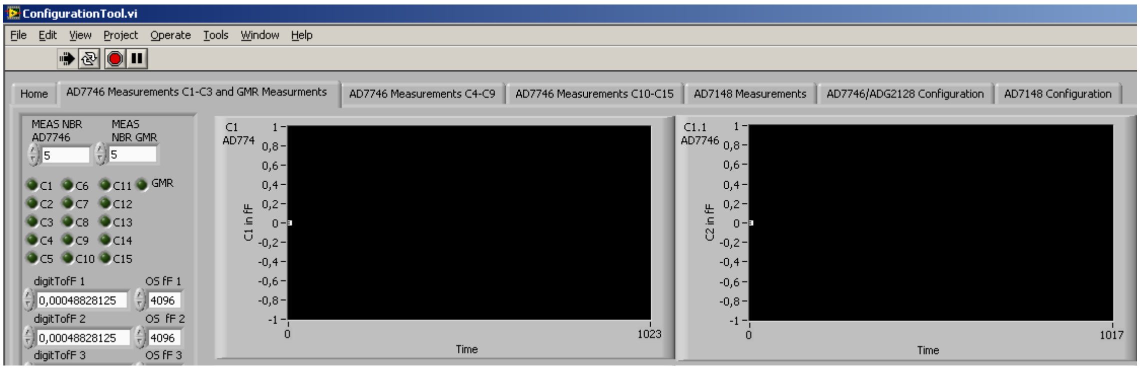

MEAS NBR AD7746: 5

MEAS NBR GMR: 5

digitTofF 1: 0,00048828125

OS fF 1: 4096

digitTofF 2: 0,00048828125

OS fF 2: 4096

digitTofF 3

OS fF 3

Figure A.2: Image section of second page 'AD7746 measurements C1-C3 and GMR measurements'. At the top left, the number of measurements per data package is selectable for AD7746 and GMR sensors. Due to the maximum package size of 50 bytes the maximum number of measurements per data package is five for both the AD7746 and the GMR sensors. Up to 15 capacitances (C1-C15) and up to two GMR sensor signals can be evaluated at the same time. Each LED, waveform chart and input box (e.g., 'dialogTofF 1' and 'OS fF 1') is assigned to a certain data package. For example, a data package of AD7746 arrives containing measurement data C1. In this case, LED C1 flashes, the data is converted by 'dialogTofF 1' (multiply factor) and 'OS fF 1' (offset correction) and the waveform charts C1 and C1.1 (counter measurement of C1) are updated. The counter measurement is defined as follows. For example C1 is the capacitance measured between electrode 2 and 3. Then the corresponding counter measurement C1.1 is the capacitance measured between electrodes 3 and 2. The waveform charts for C1-C3 of AD7746 and the two GMR measurements are on this page. The third and fourth page (AD7746 measurements C4 - C9 and C10 - C15) contain the waveform charts for the capacitances C4 - C15 of AD7746.

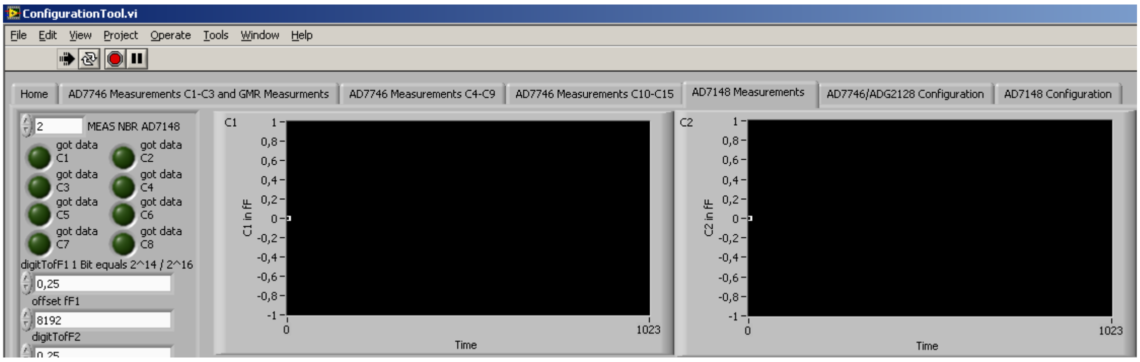

MEAS NBR AD7148: 2

digitTofF1 1 Bit equals 2^14 / 2^16: 0,25

offset fF1: 8192

digitTofF2: 0,25

Figure A.3: Image section of fifth page 'AD7148 measurements'. The maximum number of measurements per data package is two for the AD7148. All eight conversation stages (capacitances C1 - C8) of the AD7148 can be displayed. The received data packages for the AD7148 are converted and illustrated in the same way as described in Figure A.2 for AD7746.

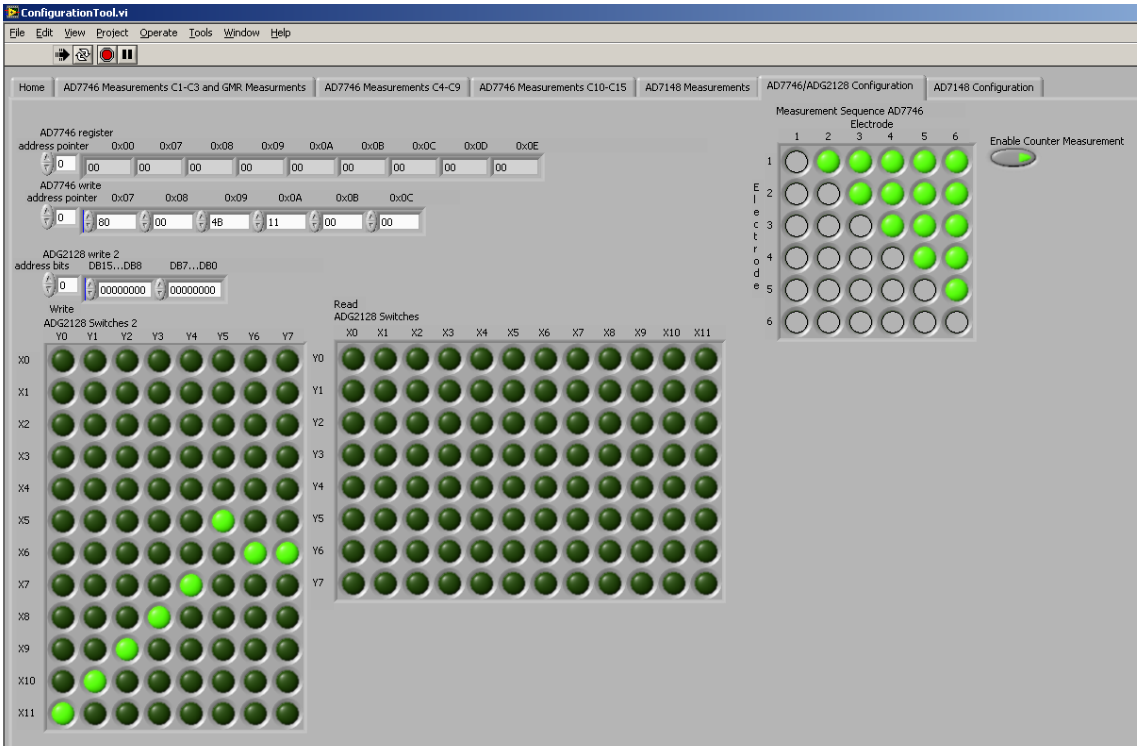

AD7746 register

address pointer	0x00	0x07	0x08	0x09	0x0A	0x0B	0x0C	0x0D	0x0E
0	00	00	00	00	00	00	00	00	00

AD7746 write

address pointer	0x07	0x08	0x09	0x0A	0x0B	0x0C
0	80	00	4B	11	00	00

ADG2128 write 2

address bits	DB15...DB8	DB7...DB0
0	00000000	00000000

Figure A.4: Image section of sixth page 'AD7746/ADG2128 configuration'. The box array 'AD7746 register' displays the read shadow/chip register configuration of AD7746. The input box 'AD7746 write' displays the data to be written to the shadow/chip register of the AD7746 if the command 'CMD_WRITE_REGISTER_AD7746' is sent. The input box 'ADG2128 write 2' displays the data to be written to the register of ADG2128 if the command CMD_WRITE_BYTES_ADG2128 is sent. The LED array 'Write ADG2128 Switches 2' depicts the switch states to be written to the shadow/chip register of the 8×12 switch matrix ADG2128 if the command CMD_WRITE_REGISTER_ADG2128 is sent. This configuration is used for the AD7148 measurement. 'Read ADG2128 Switches' depicts the read shadow/chip register of ADG2128. Each LED represents a switch of the 8×12 switch matrix ADG2128. At the top right, 'Measurement Sequence AD7746' depicts the measurement sequence for the AD7746 measurement. Up to 15 capacitances are selectable. The button 'Enable counter measurement' enables counter measurement for the selected capacitance. Each LED depicts a single capacitance between two electrodes. The sequence number is assigned to the number of enabled LEDs starting at the top left going line by line from left to right. For example, the LED in row three and column five is the measured capacitance between electrodes three and five and has the sequence number eleven. Thus, the measured capacitance is displayed in the wave chart C11 and the counter measurement in C11.1. Another example is given in Figure A.5.

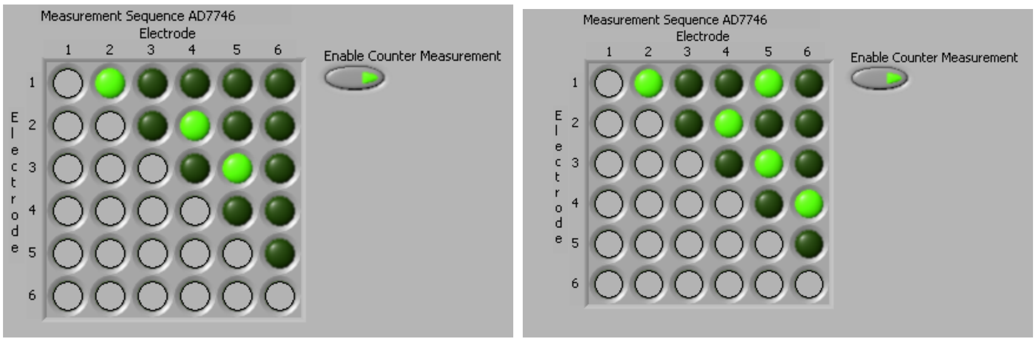

(a) (b)

Figure A.5: Two configuration examples of AD7746 measurement sequences. (a) Three capacitances are measured. The sequence number is assigned to the number of enabled LEDs starting at the top left going line by line from left to right. For example, the LED in row three and column five is assigned to sequence number three measuring the capacitance between electrodes three and five. According to the sequence number the data is displayed in the wave charts C3 and C3.1. (b) In this case the LED in row three and column five is assigned to sequence number four. Therefore, the data is displayed in the wave charts C4 and C4.1. The six electrodes are connected to the switch matrix starting from port Y0 to Y5, e.g., electrodes 2 is connected to port Y1 (see Figure B.2).

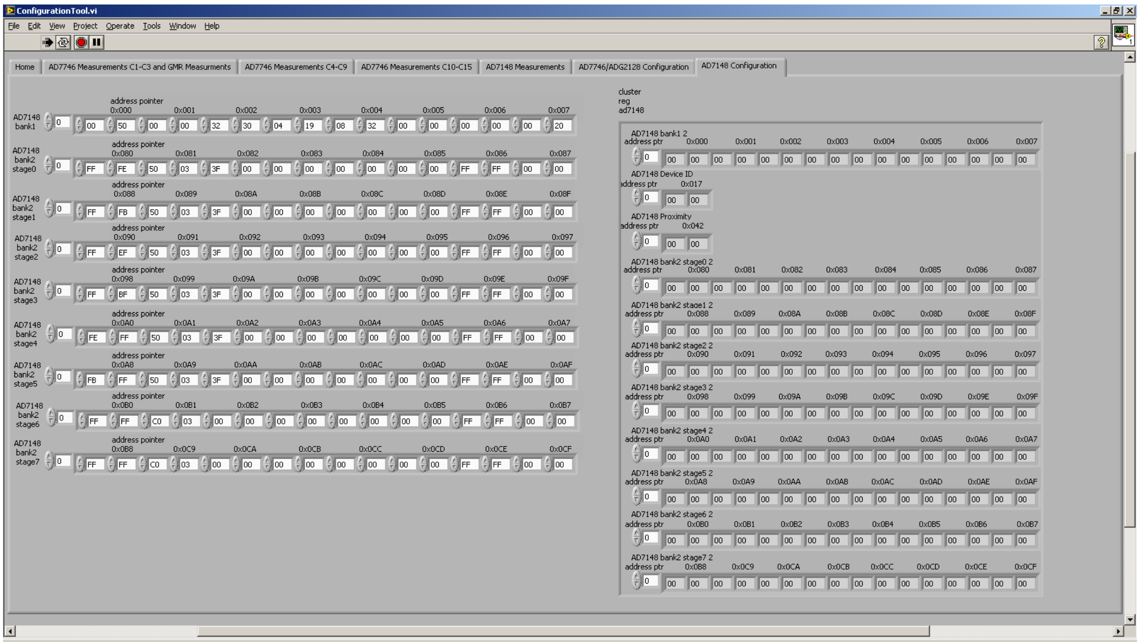

	address pointer							
AD7148 bank1	0	0x000 00 50	0x001 00 00	0x002 32 30	0x003 04 19	0x004 08 32	0x005 00 00	0x006 00 00	0x007 00 20
AD7148 bank2 stage0	0	0x080 FF FE	0x081 50 03	0x082 3F 00	0x083 00 00	0x084 00 00	0x085 00 00	0x086 FF FF	0x087 00 00
AD7148 bank2 stage1	0	0x088 FF FB	0x089 50 03	0x08A 3F 00	0x08B 00 00	0x08C 00 00	0x08D 00 00	0x08E FF FF	0x08F 00 00
AD7148 bank2 stage2	0	0x090 FF EF	0x091 50 03	0x092 3F 00	0x093 00 00	0x094 00 00	0x095 00 00	0x096 FF FF	0x097 00 00
AD7148 bank2 stage3	0	0x098 FF BF	0x099 50 03	0x09A 3F 00	0x09B 00 00	0x09C 00 00	0x09D 00 00	0x09E FF FF	0x09F 00 00
AD7148 bank2 stage4	0	0x0A0 FE FF	0x0A1 50 03	0x0A2 3F 00	0x0A3 00 00	0x0A4 00 00	0x0A5 00 00	0x0A6 FF FF	0x0A7 00 00
AD7148 bank2 stage5	0	0x0A8 FB FF	0x0A9 50 03	0x0AA 3F 00	0x0AB 00 00	0x0AC 00 00	0x0AD 00 00	0x0AE FF FF	0x0AF 00 00
AD7148 bank2 stage6	0	0x0B0 FF FF	0x0B1 C0 03	0x0B2 00 00	0x0B3 00 00	0x0B4 00 00	0x0B5 00 00	0x0B6 FF FF	0x0B7 00 00
AD7148 bank2 stage7	0	0x0B8 FF FF	0x0C9 C0 03	0x0CA 00 00	0x0CB 00 00	0x0CC 00 00	0x0CD 00 00	0x0CE FF FF	0x0CF 00 00

cluster
reg
ad7148

	address ptr								
AD7148 bank1 2	0	0x000 00 00	0x001 00 00	0x002 00 00	0x003 00 00	0x004 00 00	0x005 00 00	0x006 00 00	0x007 00 00
AD7148 Device ID	0	0x017 00 00							
AD7148 Proximity	0	0x042 00 00							
AD7148 bank2 stage0 2	0	0x080 00 00	0x081 00 00	0x082 00 00	0x083 00 00	0x084 00 00	0x085 00 00	0x086 00 00	0x087 00 00
AD7148 bank2 stage1 2	0	0x088 00 00	0x089 00 00	0x08A 00 00	0x08B 00 00	0x08C 00 00	0x08D 00 00	0x08E 00 00	0x08F 00 00
AD7148 bank2 stage2 2	0	0x090 00 00	0x091 00 00	0x092 00 00	0x093 00 00	0x094 00 00	0x095 00 00	0x096 00 00	0x097 00 00
AD7148 bank2 stage3 2	0	0x098 00 00	0x099 00 00	0x09A 00 00	0x09B 00 00	0x09C 00 00	0x09D 00 00	0x09E 00 00	0x09F 00 00
AD7148 bank2 stage4 2	0	0x0A0 00 00	0x0A1 00 00	0x0A2 00 00	0x0A3 00 00	0x0A4 00 00	0x0A5 00 00	0x0A6 00 00	0x0A7 00 00
AD7148 bank2 stage5 2	0	0x0A8 00 00	0x0A9 00 00	0x0AA 00 00	0x0AB 00 00	0x0AC 00 00	0x0AD 00 00	0x0AE 00 00	0x0AF 00 00
AD7148 bank2 stage6 2	0	0x0B0 00 00	0x0B1 00 00	0x0B2 00 00	0x0B3 00 00	0x0B4 00 00	0x0B5 00 00	0x0B6 00 00	0x0B7 00 00
AD7148 bank2 stage7 2	0	0x0B8 00 00	0x0C9 00 00	0x0CA 00 00	0x0CB 00 00	0x0CC 00 00	0x0CD 00 00	0x0CE 00 00	0x0CF 00 00

Figure A.6: Seventh page 'AD7148 configuration'. The input boxes on the right-hand side display the read shadow/chip register configuration of AD7148. The input boxes on the left-hand side display the data to be written to the shadow/chip register of AD7148 if the command CMD_WRITE_REGISTER_AD7148 is sent.

CMD to send	**ID**	**Description**
CMD_STOP	0	Stops the current measurement sequence. State machine is idle.
CMD_START_GMR	1	Starts consecutive GMR measurement sequence.
CMD_START_CAP_AD7746	2	Starts consecutive AD7746 measurement sequence using shadow register configuration.
CMD_START_CAP_AD7148	3	Starts consecutive AD7148 measurement sequence using shadow register configuration.
CMD_START_BOTH_CAP	4	Starts consecutive AD7746 and AD7148 measurement sequence using shadow register configuration.
CMD_START_ALL	5	Starts consecutive AD7746, AD7148 and GMR measurement sequence using shadow register configuration.
CMD_TEST	6	Test sequence to receive predefined data packets for debugging.
CMD_READ_REGISTER_AD7746	7	Reads shadow register / register of AD7746 (depends on state of read through button).
CMD_WRITE_REGISTER_AD7746	8	Writes shadow register / register of AD7746 (depends on state of write through button).
CMD_READ_REGISTER_ADG2128	9	Reads shadow register / register of ADG2128 (depends on state of read through button).
CMD_WRITE_REGISTER_ADG2128	10	Writes shadow register / register of ADG2128 (depends on state of write through button).
CMD_WRITE_BYTES_ADG2128	11	Writes byte sequence to register of ADG2128.
CMD_READ_REGISTER_AD7148	12	Reads shadow register / register of AD7148 (depends on state of read through button).
CMD_WRITE_REGISTER_AD7148	13	Writes shadow register / register of AD7148 (depends on state of write through button).
CMD_SW_RESET_AD7746	14	Software reset of AD7148.
CMD_SETUP_ADG2128_SEQUENCE	15	Setup ADG2128 sequence for AD7746 measurement.

Table A.1: Selectable commands of drop down menu 'CMD to send'. The ID corresponds to the ID of Table A.3.

A.1.1 Configuration Examples

First, the prototype has to be connected to the host computer properly as described in Section A.3. Then, the configuration process can be started using the CT. It should be noted that a running measurement sequence must be stopped by sending the command 'CMD_STOP' in advance.

AD7746

First, the AD7746 measurement sequence has to be set up by sending the command CMD_SETUP_ADG2128_SEQUENCE. The sequence can be selected at 'Measurement sequence AD7746' on page six of the CT. Second, the register configuration has to be written to the AD7746 by sending the command CMD_WRITE_REGISTER_AD7746. The register configuration can be altered at 'AD7746 write' on page six of the CT. Finally, the measurement sequence can be started by sending the command CMD_START_CAP_AD7746. This command sequence is required to start the measurement sequence properly.

AD7148

First, the switch matrix ADG2128 has to be set up by sending the command CMD_WRITE_REGISTER_ADG2128. The switch configuration can be selected at 'Write ADG2128 Switches 2' on page six of the CT. Second, the register configuration has to be written to the AD7148 by sending the command CMD_WRITE_REGISTER_AD7148. The register configuration can be altered at 'AD7148 bank1 - bank2' on page six of the CT. Finally, the measurement sequence can be started by sending the command CMD_START_CAP_AD7148. This command sequence is required to start the measurement sequence properly.

GMR

The measurement sequence can be started by sending the command CMD_START_GMR.

A.2 CCS Project: ObjRecLocV1

A.2.1 Transmitter Module

The build configuration 'Transmitter((LinkTo))' and 'TransmitterSerial' are developed for the TM of the measurement setup shown in Figures 4.3(a) and 4.3(b). A finite state machine is implemented to process the received commands. The state machine checks if a new command is received. Once a new command has arrived the state machine switches to the dedicated state to process the command. Otherwise the state machine checks if a consecutive measurement is running and switches to the dedicated state to continue the measurement if needed (see Figure A.8). The state diagram is shown in Figure A.7 and the states are listed below.

- START_UP Initialize the finite state machine.
- IDLE Checks whether new command is received. Switches state if new command is received or a consecutive measurement is running.
- MEASUREMENT_CAP_AD7746 Consecutive measurement AD7746. This state can switch to MEASUREMENT_CAP_AD7148 if command CMD_START_BOTH_CAP or CMD_START_ALL was received.
- MEASUREMENT_CAP_AD7148 Consecutive measurement AD7148.
- MEASUREMENT_GMR Consecutive measurement GMR. This state can switch to MEASUREMENT_CAP_AD7746 if command CMD_START_ALL was received.
- READ_REGISTER_AD7746 Read register of AD7746 and returns to state IDLE.
- WRITE_REGISTER_AD7746 Write register of AD7746 and returns to state IDLE.
- READ_REGISTER_ADG2128 Read register of ADG2128 and returns to state IDLE.
- WRITE_REGISTER_ADG2128 Write register of ADG2128 and returns to state IDLE.
- WRITE_BYTES_ADG2128 Write register of ADG2128 and returns to state IDLE.
- READ_REGISTER_AD7148 Read register of AD7148 and returns to state IDLE.
- WRITE_REGISTER_AD7148 Write register of AD7148 and returns to state IDLE.
- SETUP_ADG2128_SEQUENCE Write measurement sequence for AD7746 to shadow register and returns to state IDLE.

A.2.2 Receiver Module

The build configuration 'Receiver ((LinkListen))' is dedicated for the receiver module of the measurement setup shown in Figure 4.3(a). The software running on the receiver is based on a simple buffered data receiving and forwarding principle. Packets received via the serial interface from the host computer are positively acknowledged when the data is successfully forwarded via the RF link, otherwise a not acknowledge is sent to the host

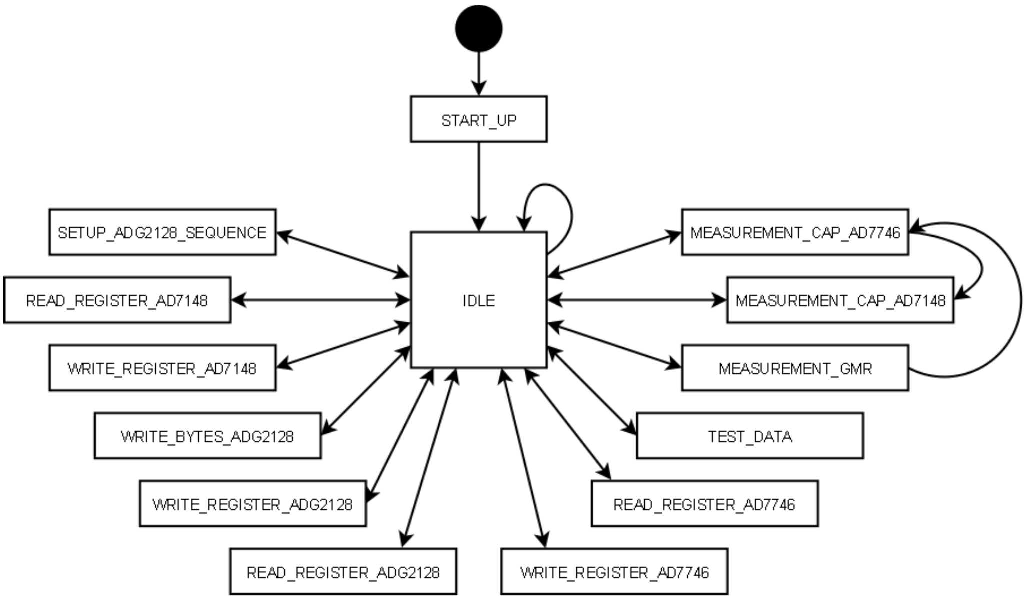

Figure A.7: State machine of the TM

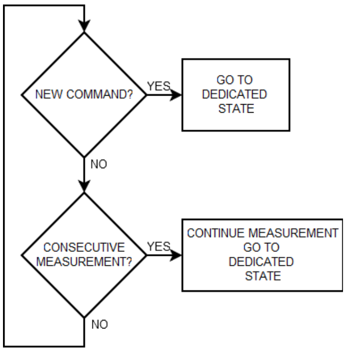

Figure A.8: State IDLE

computer. Data received via the RF link from the TM is forwarded to the host computer without acknowledgment.

A.3 Setup Prototype

The sensors GMR 1 and GMR 2 should be connected to Port 2.0 and Port 2.1 of the TM. The electrodes 1 - 6 (see Figure 3.2) should be connected to Y0 - Y5 of the capacitive measurement PCB shown in Figures B.2 and B.3(a).

The software for the microcontroller boards EM430F6137RF900 was developed with the Code Composer Studio (CCS) and SimpliciTI from Texas Instruments. To compile and execute the project 'ObjRecLocV1' it is necessary to copy the project folder 'ObjRecLocV1' and the SimpliciTI folder 'Components' into the workspace directory of the CSS. The path variable named DEV_ROOT1 must be set to the SimpliciTI folder 'Components' and the project 'ObjRecLocV1' can be imported in the CSS (the folder 'LinkedComponents' must be deleted if the folder shows up in the project tree of the CCS). The path variable is necessary to link all required files from SimpliciTI. Within the project three different build configurations can be selected.

To set up the prototype as shown in Figure 4.3(a), follow the given instructions.
To set up the TM download the build configuration 'Transmitter((LinkTo))' to the microcontroller board. It should be noted that the macro RADIO_COMMUNICATION in the file *constants.h* of the CCS project 'ObjRecLocV1' must be defined. Connect the USB to UART converter to Port 2.4 (TX) and 2.2 (RX) of the receiver module. To set up the receiver module, download the build configuration 'Receiver ((LinkListen))' to the microcontroller board. Once this is done, press button S2 on the TM. The TM tries to establish an RF link to the receiver module by transmitting a broadcast link frame. While the TM is waiting for a reply the green and red LEDs are flashing. Next, press button S2 on the receiver module. The receiver module starts listening for a broadcast link frame. If the receiver module receives the broadcast, a reply is sent to the transmitter and the green LED flashes once. At the TM the green and red LEDs stop flashing to indicate that the connection is established and the state machine is up and running.
To set up the prototype as shown in Figure 4.3(b), follow the given instructions.
Connect the USB to UART converter to Port 3.7 (TX) and 3.5 (RX) of the TM. Comment the macro RADIO_COMMUNICATION in the file *constants.h* of the CCS project 'ObjRecLocV1' and download the build configuration 'TransmitterSerial' to the TM. To start the state machine press button S2.

A.4 Matlab Scripts

Once the setup and the configuration of the prototype is done as described in Sections A.1.1 and A.3 the reconstruction can be started. It should be noted that the CT should be used to configure AD7746, AD7148 and ADG2128. However, the measurement sequences should not be started in the CT because this is done automatically in MATLAB. Once the configuration is finished, make sure that LabView does not block the serial port anymore before starting the MATLAB scripts.
To start a reconstruction process the MATLAB script *scriptRunReco.m* provides the following functionality:

- Run the online reconstruction $\mathrm{ECT}_{\mathrm{BFGS}}$ or $\mathrm{ECT}_{\mathrm{GIBBS}}$ as standalone application.

- Run the online reconstruction $\mathrm{ECT}_{\mathrm{BFGS}}$ and MSS or $\mathrm{ECT}_{\mathrm{GIBBS}}$ and MSS simultaneously.

To generate the necessary files to run a reconstruction the scripts *scriptInitialization.m* (generate mesh file) and *scriptReferenceMeasurement.m* (read calibration files) can be used. To start the MSS as a standalone application the MATLAB script *gmrOnline.m* is provided. To generate a calibration file for the MSS the file *scriptReadSimulationData.m* can be used.

A.5 Configuration Messages From Client Application to Transmitter Module

The configuration messages from the CA to TM are used within the CT and MATLAB scripts to set up the microcontroller board, IC's (AD7746, AD7148, ADG2128) and to start measurement sequences.

	Header	**Data**
Byte	0 - 4	5 - 49

Table A.2: Configuration Messages from CA to TM. The number of data bytes depends on the message to be sent.

A.5.1 Header

	Header				
Byte	0	1	2	3	4
Mnemonic	ID	DATA FLAG	PKG LENGTH	NBR PKG	CUR PKG NBR

Table A.3: Header: configuration message from CA to TM.

Byte	**Mnemonic**	**Description**
0	ID	Unique identifier of configuration message
1	DATA FLAG	1 if length of Data is > 0 otherwise 0
2	PKG LENGTH	Length of current package
3	NBR PKG	Number of packages of current message
4	CUR PKG NBR	Current package number to transmit

Table A.4: Description header: configuration message from CA to TM.

A.5.2 Data

Commands to Start Measurement Sequences

	Data
Byte	5
Mnemonic	NBR MEAS

Table A.5: Data: start measurement sequence of either GMR, AD7746 or AD7148 from CA to TM.

Byte	**Mnemonic**	**Description**
5	NBR MEAS	Number of measurements per data package.

Table A.6: Description data: start measurement sequences of either GMR, AD7746 or AD7148 from CA to TM.

	Data	
Byte	5	6
Mnemonic	NBR MEAS AD7746	NBR MEAS AD7148

Table A.7: Data: start measurement sequence AD7746 and AD7148 from CA to TM.

Byte	**Mnemonic**	**Description**
5	NBR MEAS AD7746	Number of measurements per data package AD7746.
6	NBR MEAS AD7148	Number of measurements per data package AD7148.

Table A.8: Description data: start measurement sequence AD7746 and AD7148 from CA to TM.

	Data		
Byte	5	6	7
Mnemonic	NBR MEAS AD7746	NBR MEAS AD7148	NBR MEAS GMR

Table A.9: Data: start measurement sequence all (GMR, AD7746 and AD7148) from CA to TM.

Byte	**Mnemonic**	**Description**
5	NBR MEAS AD7746	Number of measurements per data package AD7746.
6	NBR MEAS AD7148	Number of measurements per data package AD7148.
7	NBR MEAS GMR	Number of measurements per data package GMR.

Table A.10: Description data: start measurement sequence all (GMR, AD7746 and AD7148) from CA to TM.

AD7746

	Data				
Byte	5	6	7	8	9
Mnemonic	WTF	CAP SETUP	VT SETUP	EXC SETUP	CONFIG
Byte	10	11			
Mnemonic	CAP DAC A	CAP DAC B			

Table A.11: Data: AD7746 write register message from CA to TM.

Byte	**Mnemonic**	**Description**
5	WTF	Write through flag: 1 Writes data into shadow register and AD7746 register 0 Writes data into shadow register
6	CAP SETUP	Capacitive channel setup register [Ana05]
7	VT SETUP	Voltage and temperature channel setup register [Ana05]
8	EXC SETUP	Capacitive channel excitation setup register [Ana05]
9	CONFIG	Configuration register [Ana05]
10	CAP DAC A	Capacitive DAC A setup register [Ana05]
11	CAP DAC B	Capacitive DAC B setup register [Ana05]

Table A.12: Description data: AD7746 write register message from CA to TM.

	Data
Byte	5
Mnemonic	RTF

Table A.13: Data: AD7746 read register message from CA to TM

Byte	Mnemonic	Description
5	RTF	Read through flag: 1 reads data from chip register (writes data implicitly into shadow register) 0 reads data from shadow register

Table A.14: Description data: AD7746 read register message from CA to TM.

ADG2128

	Data												
Byte	5	6	7	8	9	10	11	12	13	14	15	16	17
Mnemonic	WTF	X0	X1	X2	X3	X4	X5	X6	X7	X8	X9	X10	X11

Table A.15: Data: ADG2128 write switch configuration message for AD7746 measurement from CA to TM.

Byte	Mnemonic	Description
5	WTF	Write through flag: 1 Writes data into shadow register and ADG2128 register 0 Writes data into shadow register
6	X0	Switch configuration X0 (DB8 to DB15) of ADG2128 [Ana06]
7	X1	Switch configuration X1 (DB8 to DB15) of ADG2128 [Ana06]
8	X2	Switch configuration X2 (DB8 to DB15) of ADG2128 [Ana06]
9	X3	Switch configuration X3 (DB8 to DB15) of ADG2128 [Ana06]
10	X4	Switch configuration X4 (DB8 to DB15) of ADG2128 [Ana06]
11	X5	Switch configuration X5 (DB8 to DB15) of ADG2128 [Ana06]
12	X6	Switch configuration X6 (DB8 to DB15) of ADG2128 [Ana06]
13	X7	Switch configuration X7 (DB8 to DB15) of ADG2128 [Ana06]
14	X8	Switch configuration X8 (DB8 to DB15) of ADG2128 [Ana06]
15	X9	Switch configuration X9 (DB8 to DB15) of ADG2128 [Ana06]
16	X10	Switch configuration X10 (DB8 to DB15) of ADG2128 [Ana06]
17	X11	Switch configuration X11 (DB8 to DB15) of ADG2128 [Ana06]

Table A.16: Description data: ADG2128 write switch configuration message for AD7746 measurement from CA to TM.

	Data		
Byte	5	6	7 - 18
Mnemonic	RTF	LINE NBR	LINE ADDRESSES

Table A.17: Data: ADG2128 read switch configuration message from CA to TM.

Byte	**Mnemonic**	**Description**
5	RTF	Read through flag: 1 Reads data from chip register 0 Reads data from shadow register
6	LINE NBR	0-11: X$<\$LINE\ NBR>$ line to read 12: Read all X0-X12 lines
7 - 18	LINE ADDRESSES	Read back addresses for each X line to read. Only necessary if RTF is set. See [Ana06]

Table A.18: Description data: ADG2128 read switch configuration message from CA to TM.

	Data							
Byte	5	6	7	8	9	10	11	12
Mnemonic	SEQ LENGTH	CM FLAG	E1	E2	E3	E4	E5	E6

Table A.19: Data: ADG2128 sequence of switch configurations message from CA to TM.

Byte	**Mnemonic**	**Description**
5	SEQ LENGTH	Length of switch configuration sequence
6	CM FLAG	Counter-measurement flag: 1 Counter-measurement is enabled 0 Counter-measurement is disabled
7	E1	Electrode 1 configuration of sequence
8	E2	Electrode 2 configuration of sequence
9	E3	Electrode 3 configuration of sequence
10	E4	Electrode 4 configuration of sequence
11	E5	Electrode 5 configuration of sequence
12	E6	Electrode 6 configuration of sequence

Table A.20: Description data: ADG2128 sequence of switch configurations message from CA to TM.

AD7148

	Data
Byte	5
Mnemonic	RTF

Table A.21: Data: AD7148 read register message from CA to TM.

Byte	**Mnemonic**	**Description**
5	RTF	Read through flag: 1 reads data from chip register (writes data implicitly into shadow register) 0 reads data from shadow register

Table A.22: Description data: AD7148 read register message from CA to TM.

	Data			
Byte	5	6 - 7	8 - 15	16 - 21
Mnemonic	WTF	SETUP CONTROL	CAL SETUP	INT ENABLE

Table A.23: Data: first package of AD7148 write register message from CA to TM.

Byte	**Mnemonic**	**Description**
5	WTF	Write through flag: 1 Writes data into shadow register and ad7746 register 0 Writes data into shadow register
6 - 7	SETUP CONTROL	Register bank 1: $PWR\_CONTROL$ register [Ana10]
8 - 15	CAL SETUP	Register bank 1: $STAGEx\_CAL\_EN$, AMB_COMP_CTRL0, AMB_COMP_CTRL1 and AMB_COMP_CTRL2 register [Ana10]
16 - 21	INT ENABLE	Register bank 1: $STAGEx\_LOW\_INT\_EN$, $STAGEx\_HIGH\_INT\_EN$ and $STAGEx\_COMPLETE\_INT\_EN$ register [Ana10]

Table A.24: Description data: first package of AD7148 write register message from CA to TM.

	Data		
Byte	5	6 - 21	22 - 37
Mnemonic	WTF	STAGE 0	STAGE 1

Table A.25: Data: second package of AD7148 write register message from CA to TM.

Byte	Mnemonic	Description
5	WTF	Write through flag: 1 Writes data into shadow register and ad7746 register 0 Writes data into shadow register
6 - 21	STAGE 0	Register bank 2: $STAGE0$ configuration register [Ana10]
22 - 37	STAGE 1	Register bank 2: $STAGE1$ configuration register [Ana10]

Table A.26: Description data: second data package of write register message of AD7148 from CA to TM.

	Data		
Byte	5	6 - 21	22 - 37
Mnemonic	WTF	STAGE 2	STAGE 3

Table A.27: Data: third package of AD7148 write register message from CA to TM.

Byte	Mnemonic	Description
5	WTF	Write through flag: 1 Writes data into shadow register and ad7746 register 0 Writes data into shadow register
6 - 21	STAGE 2	Register bank 2: $STAGE2$ configuration register [Ana10]
22 - 37	STAGE 3	Register bank 2: $STAGE3$ configuration register [Ana10]

Table A.28: Description data: third data package of write register message of AD7148 from CA to TM.

	Data		
Byte	5	6 - 21	22 - 37
Mnemonic	WTF	STAGE 4	STAGE 5

Table A.29: Data: fourth package of AD7148 write register message from CA to TM.

Byte	Mnemonic	Description
5	WTF	Write through flag: 1 Writes data into shadow register and ad7746 register 0 Writes data into shadow register
6 - 21	STAGE 4	Register bank 2: $STAGE4$ configuration register [Ana10]
22 - 37	STAGE 5	Register bank 2: $STAGE5$ configuration register [Ana10]

Table A.30: Description data: fourth data package of write register message of AD7148 from CA to TM.

	Data		
Byte	5	6 - 21	22 - 37
Mnemonic	WTF	STAGE 6	STAGE 7

Table A.31: Data: fifth package of AD7148 write register message from CA to TM.

Byte	Mnemonic	Description
5	WTF	Write through flag: 1 Writes data into shadow register and ad7746 register 0 Writes data into shadow register
6 - 21	STAGE 6	Register bank 2: $STAGE6$ configuration register [Ana10]
22 - 37	STAGE 7	Register bank 2: $STAGE7$ configuration register [Ana10]

Table A.32: Description data: fifth data package of write register message of AD7148 from CA to TM.

A.6 Configuration Messages From Transmitter Module to Client Application

The configuration messages from the transmitter module to the client application are the reply messages from the transmitter module to the configuration messages described in the previous Section A.5.

	Header	Data
Byte	0 - 3	4 - (max.) 49

Table A.33: Configuration Messages from TM to CA. The number of data bytes depends on the message to be sent.

A.6.1 Header

	Header
Byte	0 - 3
Mnemonic	IDENTIFIER

Table A.34: Header: configuration message from TM to CA.

Byte	**Mnemonic**	**Description**
0 - 3	IDENTIFIER	Identifier of configuration message

Table A.35: Description header: configuration message from TM to CA.

A.6.2 Data

AD7746

	Data				
Byte	4	5	6	7	8
Mnemonic	ID	STATUS	CAP SETUP	VT SETUP	EXC SETUP
Byte	9	10	11	12	13
Mnemonic	CONFIG	CAP DAC A	CAP DAC B	CAP OFFSET H	CAP OFFSET L

Table A.36: Reply message of AD7746 write register message from TM to CA.

Byte	Mnemonic	Description
4	ID	Unique identifier for AD7746 data
5	STATUS	Content of status register [Ana05]
6	CAP SETUP	Content of capacitive channel setup register [Ana05]
7	VT SETUP	Content of voltage and temperature channel setup register [Ana05]
8	EXC SETUP	Content of capacitive channel excitation setup register [Ana05]
9	CONFIG	Content of configuration register [Ana05]
10	CAP DAC A	Content of capacitive DAC A setup register [Ana05]
11	CAP DAC B	Content of capacitive DAC B setup register [Ana05]
12	CAP OFFSET H	Content of high byte of capacitive offset calibration register [Ana05]
13	CAP OFFSET L	Content of low byte of capacitive offset calibration register [Ana05]

Table A.37: Description: reply message of AD7746 write register message from TM to CA.

ADG2128

	Data	
Byte	4	5 - 16
Mnemonic	ID	LINE

Table A.38: Reply message of ADG2128 read switch configuration message from TM to CA.

Byte	Mnemonic	Description
4	ID	Unique identifier for ADG2128 data
5 - (max.) 16	LINE	Current switch configuration of line(s) to be read.

Table A.39: Description: reply message of ADG2128 read switch configuration message from TM to CA.

AD7148

	Data			
Byte	4	5	6	7 - 8
Mnemonic	ID	NBR PKG	CUR PKG NBR	SETUP CONTROL
Byte	9 - 16	17 - 22	23 - 24	25 - 26
Mnemonic	CAL SETUP	INT ENABLE	DEVICE ID	PROXIMITY

Table A.40: Reply message: first package of AD7148 read register message from TM to CA.

Byte	Mnemonic	Description
4	ID	Unique identifier for ADG2128 data
5	NBR PKG	Number of packages of current message
6	CUR PKG NBR	Current package number to transmit
7 - 8	SETUP CONTROL	Content of register bank 1: *PWR_CONTROL* register [Ana10]
9 - 16	CAL SETUP	Content of register bank 1: *STAGEx_CAL_EN*, *AMB_COMP_CTRL*0, *AMB_COMP_CTRL*1 and *AMB_COMP_CTRL*2 register [Ana10]
17 - 22	INT ENABLE	Content of register bank 1: *STAGEx_LOW_INT_EN*, *STAGEx_HIGH_INT_EN* and *STAGEx_COMPLETE_INT_EN* register [Ana10]
23 - 24	DEVICE ID	Content of register bank 1: *Device ID* register [Ana10]
25 - 26	PROXIMITY	Content of register bank 1: *Proximity Status* register [Ana10]

Table A.41: Description reply message: first package of AD7148 read register message from TM to CA.

	Data				
Byte	4	5	6	7 - 22	23 - 38
Mnemonic	ID	NBR PKG	CUR PKG NBR	STAGE 0	STAGE 1

Table A.42: Reply message: second package of AD7148 read register message from TM to CA.

Byte	**Mnemonic**	**Description**
4	ID	Unique identifier for ADG2128 data
5	NBR PKG	Number of packages of current message
6	CUR PKG NBR	Current package number to transmit
7 - 22	STAGE 0	Content of register bank 2: $STAGE0$ configuration register [Ana10]
23 - 38	STAGE 1	Content of register bank 2: $STAGE1$ configuration register [Ana10]

Table A.43: Description reply message: second package of AD7148 read register message from TM to CA.

	Data				
Byte	4	5	6	7 - 22	23 - 38
Mnemonic	ID	NBR PKG	CUR PKG NBR	STAGE 2	STAGE 3

Table A.44: Reply message: third package of AD7148 read register message from TM to CA.

Byte	**Mnemonic**	**Description**
4	ID	Unique identifier for ADG2128 data
5	NBR PKG	Number of packages of current message
6	CUR PKG NBR	Current package number to transmit
7 - 22	STAGE 2	Content of register bank 2: $STAGE2$ configuration register [Ana10]
23 - 38	STAGE 3	Content of register bank 2: $STAGE3$ configuration register [Ana10]

Table A.45: Description reply message: third package of AD7148 read register message from TM to CA.

	Data				
Byte	4	5	6	7 - 22	23 - 38
Mnemonic	ID	NBR PKG	CUR PKG NBR	STAGE 4	STAGE 5

Table A.46: Reply message: forth package of AD7148 read register message from TM to CA.

Byte	**Mnemonic**	**Description**
4	ID	Unique identifier for ADG2128 data
5	NBR PKG	Number of packages of current message
6	CUR PKG NBR	Current package number to transmit
7 - 22	STAGE 4	Content of register bank 2: $STAGE4$ configuration register [Ana10]
23 - 38	STAGE 5	Content of register bank 2: $STAGE5$ configuration register [Ana10]

Table A.47: Description reply message: fourth package of AD7148 read register message from TM to CA.

	Data				
Byte	4	5	6	7 - 22	23 - 38
Mnemonic	ID	NBR PKG	CUR PKG NBR	STAGE 6	STAGE 7

Table A.48: Reply message: fifth package of AD7148 read register message from TM to CA.

Byte	**Mnemonic**	**Description**
4	ID	Unique identifier for ADG2128 data
5	NBR PKG	Number of packages of current message
6	CUR PKG NBR	Current package number to transmit
7 - 22	STAGE 6	Content of register bank 2: $STAGE6$ configuration register [Ana10]
23 - 38	STAGE 7	Content of register bank 2: $STAGE7$ configuration register [Ana10]

Table A.49: Description reply message: fifth package of AD7148 read register message from TM to CA.

A.7 Measurement Data Messages From Transmitter Module to Client Application

The measurement data messages from the transmitter module to the client application are sent after a measurement sequence is started.

	Header	**Data**
Byte	0 - 3	4 - 47

Table A.50: Measurement data messages from TM to CA.

A.7.1 Header

	Header
Byte	0 - 3
Mnemonic	IDENTIFIER

Table A.51: Header: measurement data messages from TM to CA. See Table A.35 for the description.

A.7.2 Data

AD7746

	Data		
Byte	4 - 23	24 - 43	44 - 47
Mnemonic	M PKG	CM PKG	BUFFER

Table A.52: Data: measurement data messages of AD7746 from TM to CA.

Byte	**Mnemonic**	**Description**
4 - 23	M PKG	Up to five capacitive measurement results, e.g., electrode A against B
24 - 43	CM PKG	Up to five capacitive counter measurement results, e.g., electrode B against A
44 - 47	BUFFER	Null filled buffer

Table A.53: Description data: measurement data messages of AD7746 from TM to CA.

AD7148

	Data	
Byte	4 - 35	36 - 47
Mnemonic	M PKG	BUFFER

Table A.54: Data: measurement data messages of AD7148 from TM to CA.

Byte	Mnemonic	Description
4 - 23	M PKG	Up to two capacitive measurement sequences (stage 0 - stage 7) results.
36 - 47	BUFFER	Null filled buffer

Table A.55: Description data: measurement data messages of AD7148 from TM to CA.

GMR Sensors

	Data		
Byte	4 - 23	24 - 43	44 - 47
Mnemonic	M PKG 1	M PKG 2	BUFFER

Table A.56: Data: measurement data messages of GMR from TM to CA.

Byte	Mnemonic	Description
4 - 23	M PKG 1	Up to five GMR sensor 1 measurement results.
24 - 43	M PKG 2	Up to five GMR sensor 2 measurement results.
44 - 47	BUFFER	Null filled buffer.

Table A.57: Description data: measurement data messages of GMR from TM to CA.

Appendix B

Hardware-related Implementation Details

This chapter presents the hardware for the prototype. Section B.1 shows the used evaluation board from TI. Sections B.2 and B.3, show the schematics, layouts and parts lists of the developed PCBs for the prototype.

B.1 EM430F6137RF900 Evaluation Module

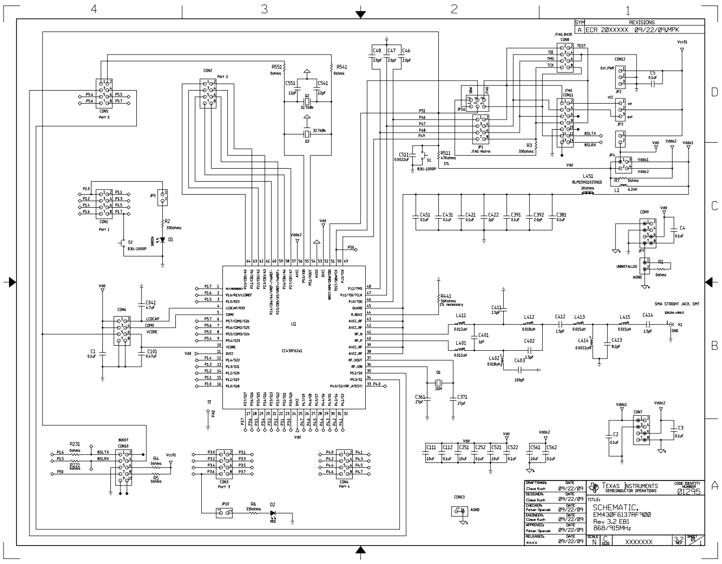

Figure B.1: Schematic of the EM430F6137RF900 evaluation module from TI [Tex10b]. For further information about the evaluation module please see [Tex10c] and [Tex10a].

B.2 Capacitive Measurement Printed Circuit Board

B.2.1 Schematic and Layouts

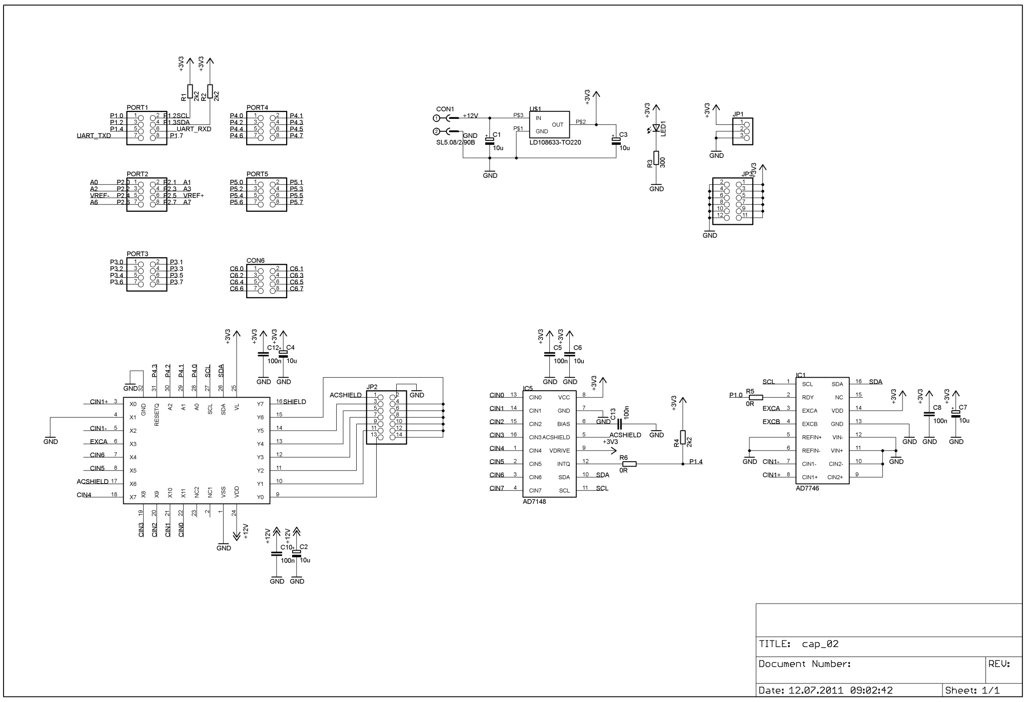

Figure B.2: Schematic of capacitive measurement PCB. Part R4 is not assembled.

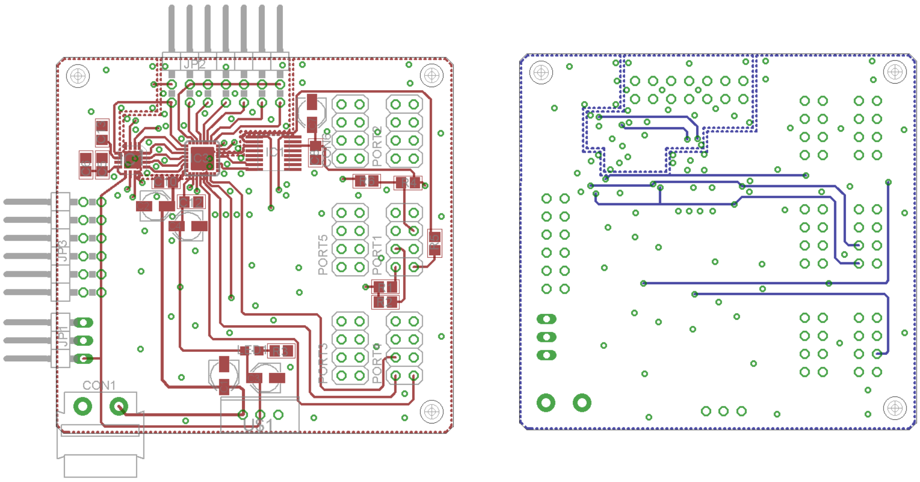

(a)

(b)

Figure B.3: (a) Top side and (b) bottom side of capacitive measurement PCB.

B.2.2 Parts List

Listing B.1: Parts list of capacitive measurement PCB

```
Partlist

Exported from cap_02.sch at 29.11.2011 10:21:31

EAGLE Version 5.11.0 Copyright (c) 1988-2010 CadSoft

Part     Value            Device            Package          Library
Sheet

C1       10u              CPOL-EUB          PANASONIC_B      rcl                1
C2       10u              CPOL-EUB          PANASONIC_B      rcl                1
C3       10u              CPOL-EUB          PANASONIC_B      rcl                1
C4       10u              CPOL-EUB          PANASONIC_B      rcl                1
C5       100n             C-EUC0805         C0805            rcl                1
C6       10u              C-EUC0805         C0805            rcl                1
C7       10u              CPOL-EUB          PANASONIC_B      rcl                1
C8       100n             C-EUC0805         C0805            rcl                1
C10      100n             C-EUC0805         C0805            rcl                1
C12      100n             C-EUC0805         C0805            rcl                1
C13      100n             C-EUC0805         C0805            rcl                1
CON1     SL5.08/2/90B     SL5.08/2/90B      SL5.08/2/90B     connector          1
CON6                      PINHD-2X4         2X04             pinhead            1
IC1      AD7746           AD7746            16-LEAD_TSSOP    AD_Capacitance     1
IC3      ADG2128          ADG2128           LFCSP32          analog-devices     1
IC5      AD7148           AD7148            MO-220-VGGC      AD_Capacitance     1
JP1                       PINHD-1X3/90      1X03/90          pinhead            1
JP2                       PINHD-2X7/90      2X07/90          pinhead            1
JP3                       PINHD-2X6/90      2X06/90          pinhead            1
LED1                      LEDCHIPLED_0805   CHIPLED_0805     led                1
PORT1                     PINHD-2X4         2X04             pinhead            1
PORT2                     PINHD-2X4         2X04             pinhead            1
PORT3                     PINHD-2X4         2X04             pinhead            1
PORT4                     PINHD-2X4         2X04             pinhead            1
PORT5                     PINHD-2X4         2X04             pinhead            1
R1       2k2              R-EU_R0805        R0805            rcl                1
R2       2k2              R-EU_R0805        R0805            rcl                1
R3       300              R-EU_R0805        R0805            rcl                1
R4       2k2              R-EU_R0805        R0805            rcl                1
R5       0R               R-EU_R0805        R0805            rcl                1
R6       0R               R-EU_R0805        R0805            rcl                1
U$1      LD108633-TO220   LD108633-TO220    TO-220           ST_spannungsregler 1
```

B.3 Giant Magnetic Resistance Sensor Printed Circuit Board

B.3.1 Schematic and Layouts

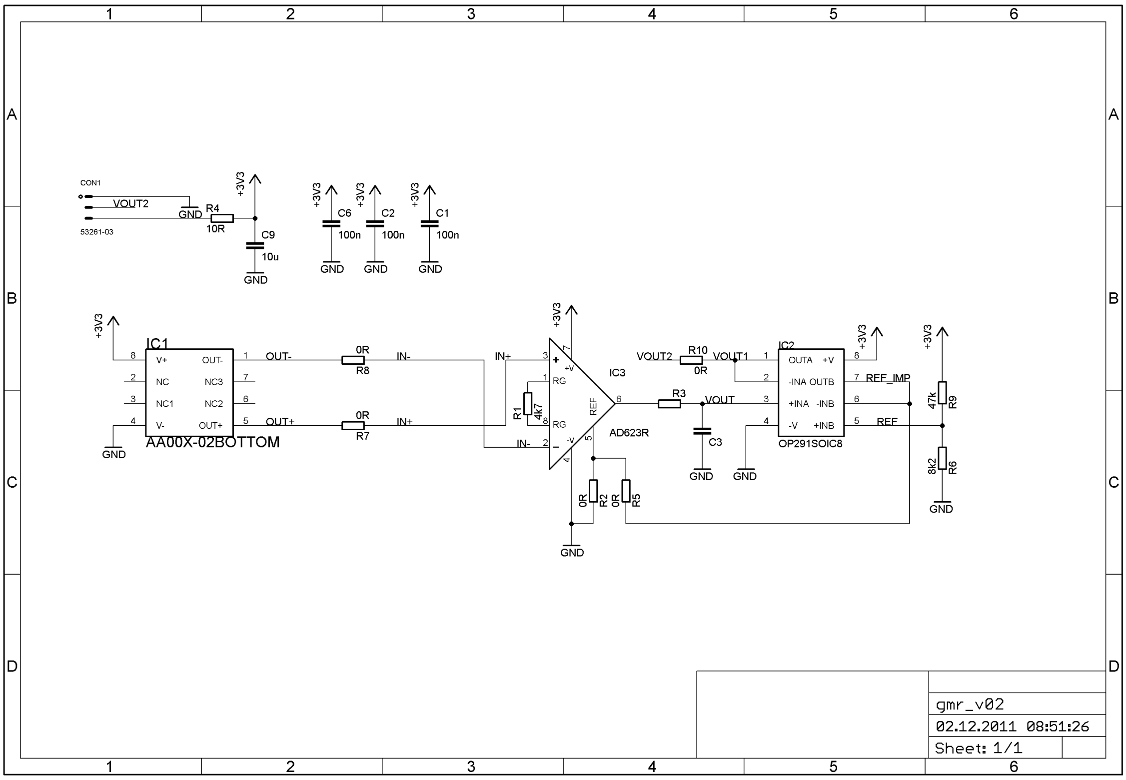

Figure B.4: Schematic of GMR PCB. Part R2, R3 and C3 are not assembled.

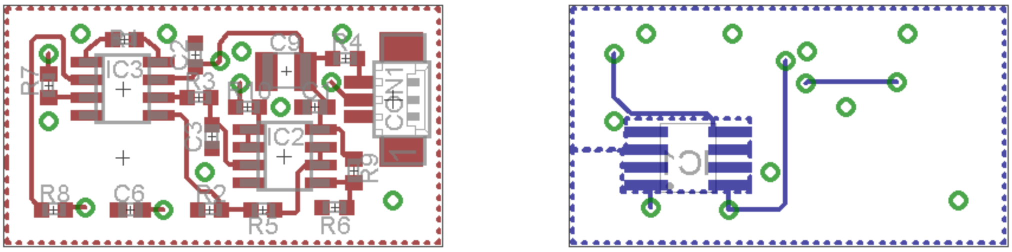

(a) (b)

Figure B.5: (a) Top side and (b) bottom side of GMR PCB.

B.3.2 Parts List

Listing B.2: Parts list of GMR PCB

```
Partlist

Exported from gmr_v02.sch at 29.11.2011 11:01:24

EAGLE Version 5.11.0 Copyright (c) 1988-2010 CadSoft

Part     Value           Device          Package        Library        Sheet

C1       100n            C-EUC0603       C0603          rcl            1
C2       100n            C-EUC0603       C0603          rcl            1
C3       1u              C-EUC0603       C0603          rcl            1
C6       100n            C-EUC0603       C0603          rcl            1
C9       10u             C-EUC1210       C1210          rcl            1
CON1     53261-03        53261-03        53261-03       connector      1
IC1      AA00X-02BOTTOM  AA00X-02BOTTOM  SOIC-8_BOTTOM  gmr            1
IC2      OP291SOIC8      OP291SOIC8      SO8            analog-devices 1
IC3      AD623R          AD623R          SO8            analog-devices 1
R1       10k             R-EU_R0603      R0603          rcl            1
R2       0R              R-EU_R0603      R0603          rcl            1
R3       100R            R-EU_R0603      R0603          rcl            1
R4       10R             R-EU_R0603      R0603          rcl            1
R5       0R              R-EU_R0603      R0603          rcl            1
R6       100k            R-EU_R0603      R0603          rcl            1
R7       0R              R-EU_R0603      R0603          rcl            1
R8       0R              R-EU_R0603      R0603          rcl            1
R9       100k            R-EU_R0603      R0603          rcl            1
R10      0R              R-EU_R0603      R0603          rcl            1
```

Appendix C

Abbreviations

AC	Alternating Current
AD	Analog Device
ADC	Analog to Digital Converter
BFGS	Broyden-Fletcher-Goldfarb-Shanno
CA	Client Application
CCS	Code Composer Studio
CDC	Capacitance to Digital Converter
CM	Conditional Mean
CMD	Command
CT	Configuration Tool
ECT	Electrical Capacitance Tomography
FE	Finite Element
FEM	Finite Element Method
GMR	Giant Magneto Resistance
GP	Gaussian Process
GPR	Gaussian Process for Regression
GUI	Graphical User Interface
IC	Integrated Circuit
I^2C	Inter Integrated Circuit
LBP	Linear Back Projection
MAP	Maximum a Posteriori
MC	Monte Carlo
MCMC	Markov Chain Monte Carlo
MH	Metropolis Hastings
ML	Maximum Likelihood
MLE	Maximum Likelihood Estimator

MSG	Message
MSS	Magnetic Sensing System
OFOA	Optimal First Order Approximation
OSOA	Optimal Second Order Approximation
PCB	Printed Circuit Board
PDE	Partial Differential Equation
PDF	Probability Density Function
PVC	Polyvinyl Chloride
REG	Register
RF	Radio Frequency
RX	Receiver
PKG	Package
ROI	Region of Interest
TI	Texas Instruments
TM	Transmitter Module
TX	Transmitter
UART	Universal Asynchronous Receiver Transmitter
USB	Universal Serial Bus

List of Figures

List of Tables

Bibliography

[Ana05] Analog Devices. *AD7745/AD7746 24-Bit Capacitance-to-Digital Converter with Temperature Sensor*, 2005. Datasheet. 23, 59, 66

[Ana06] Analog Devices. *ADG2128 I2C CMOS 8x12 Unbuffered Analog Switch Array With Dual/Single Supplies*, 2006. Datasheet. 60, 61

[Ana10] Analog Devices. *AD7148 Programmable Touch Controller for Single Electrode Capacitance Sensors*, 2010. Datasheet. 23, 62, 63, 64, 67, 68, 69

[BBF$^+$88] M. N. Baibich, J. M. Broto, A. Fert, F. Nguyen Van Dau, F. Petroff, P. Etienne, G. Creuzet, A. Friederich, and J. Chazelas. Giant magnetoresistance of (001)fe/(001)cr magnetic superlattices. *Physical Review Letters*, 61:2472–2475, Nov 1988. 7

[BHW03] B. Brandstätter, G. Holler, and D. Watzenig. Reconstruction of inhomogeneities in fluids by means of capacitance tomography. *COMPEL: The International Journal for Computation and Mathematics in Electrical and Electronic Engineering*, 22:508–519, 2003. 26

[Bra07] B. Brandstätter. Inverse problems, ill-posedness and regularization – an illustratice example. *E & I Elektrotechnik und Informationstechnik*, 124:224–231, 2007. 5, 19, 24, 26

[CCK05] B. Choi, H. R. Choi, and S. Kang. Development of tactile sensor for detecting contact force and slip. In *IEEE/RSJ International Conference on Intelligent Robots and Systems*, pages 2638 – 2643, August 2005. 1

[Fle87] R. Fletscher. *Practical Methods of Optimization.* Wiley, second edition, 1987. 27

[FSO$^+$00] P.P Freitas, F Silva, N.J Oliveira, L.V Melo, L Costa, and N Almeida. Spin valve sensors. *Sensors and Actuators A: Physical*, 81:2 – 8, 2000. 7

[GBZ89] F. Saurenbach G. Binasch, P. Grünberg and W. Zinn. Enhanced magnetoresistance in layered mangetic structures with antiferromagnetic interlayer exchange. *Journal of Physical Review B: condensed matter and material physics*, 39:4828–4830, March 1989. 7

[GMR] Gmr sensor catalog. NVE corporation. www.nve.com. 8, 9, 14

[Had02] J. Hadamard. Sur les problèmes aux dérivées partielles et leur signification physique. *Princeton University Bulletin*, pages 49–52, 1902. 24

[HNH$^+$09] K. Hsiao, P. Nangeroni, M. Huber, A. Saxena, and Y. Ng. Reactive grasping using optical proximity sensors. In *IEEE International Conference on Robotics and Automation*, pages 2098–2105, May 2009. 3

[Kay93] S.M. Kay. *Fundamentals of Statistical Signal Processing: Estimation Theory*. Prentice Hall Signal Processing Series. Prentice Hall, New Jersey, 1993. 13, 14

[KS05] J. Kaipio and E. Somersalo. *Statistical and Computational Inverse Problems*, volume 160 of *Applied Mathematical Sciences*. Springer, 2005. 26, 28, 29

[MGLS09] B. Mayton, E. Garcia, L. LeGrand, and J. R. Smith. Electric field pretouch: Towards mobile manipulation. In *Robotics: Science and Systems Workshop on Mobile Manipulation and Human Environments*, June 2009. 3

[Neu11] M. Neumayer. *Accelerated Bayesian Inversion and Calibration for Electrical Tomography*. PhD thesis, Graz, University of Technology, 2011. 20, 27, 29

[NF10] M. Neumayer and C. Fox. Fast forward map framework for electrical capacitance tomography. 2010. 24, 27, 28

[NKK07] M. Hayakawa N. K. Korovkin, V. L. Chechurin. *Inverse Problems in Electric Circuits and Electromagnetics*. Springer, 2007. 5

[Nob07] The discovery of giant magnetoresitance. Compiled by the Class for Physics of the Royal Swedish Academy of Sciences, 2007. www.kva.se. 7, 8

[NXP07] NXP Semiconductors. *I^2C-bus specification and user manual*, 2007. UM10204. 23

[NZWF11] M. Neumayer, H. Zangl, D. Watzenig, and A. Fuchs. *Current Reconstruction Algorithms in Electrical Capacitance Tomography*, volume 83 of *Lecture Notes in Electrical Engineering: New Developments and Applications in Sensing Technology*, pages 65–106. Springer, 2011. 22, 25, 26

[Rob] *RoboCup*. http://www.robocup.org. 1

[RW06] C. E. Rasmussen and C. K. I. Williams. *Gaussian Process for Machine Learning.* The MIT Press, 2006. 10, 11

[Sad07] M. N. O. Sadiku. *Elements of Electromagnetics.* The Oxford Series in Electrical and Computer Engineering. Oxford University Press, New York, 2007. 5, 20, 21

[SDN08] A. Saxena, J. Driemeyer, and A. Y. Ng. Robotic grasping of noval objects using vision. *The International Journal of Robotics Research*, 27(2):157–173, February 2008. 1

[SGWK07] J. R. Smith, E. Garcia, R. Wistort, and G. Krishnamoorthy. Electric field imaging pretouch for robotic graspers. In *IEEE International Conference on Intelligent Robots and Systems*, pages 676–683, October 2007. 3

[Tex10a] Texas Instruments. *CC430 Family. User's guide*, 2010. SLAU259B. 72

[Tex10b] Texas Instruments. *MSP430 Hardware tools. User's guide*, 2010. SLAU278G. 72

[Tex10c] Texas Instruments. *MSP430x5xx/MSP430x6xx Family. User's guide*, 2010. SLAU208H. 72

[Tho57] W. Thomson. On the electro-dynamic qualities of metals: Effects of magnetization on the electric conductivity of nickel and iron. In *Proceedings of the Royal Society of London*, pages 546 – 550, August 1856-1857. 7

[Weg06] H. Wegleiter. *LinkLow-Z carrier frequency front-end for electrical capacitance tomography applications.* PhD thesis, Graz, University of Technology, 2006. 19